Performance Limit and Design Strategy of Black Phosphorus Field-Effect Transistors

by

Demin Yin

A thesis
presented to the University of Waterloo
in fulfillment of the
thesis requirement for the degree of
Master of Applied Science
in
Electrical and Computer Engineering - Nanotechnology

Waterloo, Ontario, Canada, 2016

AUTHOR'S DECLARATION

I hereby declare that I am the sole author of this thesis. This is a true copy of the thesis, including any required final revisions, as accepted by my examiners.

I understand that my thesis may be made electronically available to the public.

Abstract

Recently, a novel two-dimensional (2D) semiconductor of few-layer black phosphorus (BP) or phosphorene has been explored extensively for future electronic device applications. BP field-effect transistors (FETs) exhibited promising device characteristics such as high field-effect mobility (μ_{eff} > 1,000 cm^2/V-s), large on current (I_{on} ~300 μA/μm), and large on-off current ratio (I_{on}/I_{off} > 10^8). In principle, the performance of BP FETs can be further improved by scaling the device, but their performance limit has not been explored particularly for multilayer BP FETs. In addition, most BP devices were studied individually without performing optimization in material or device parameters, and therefore, comprehensive design strategies for different target applications are currently absent. In this thesis, performance limit and design strategy of phosphorene FETs will be discussed by means of self-consistent atomistic quantum transport simulations using non-equilibrium Green's function (NEGF) formalism.

First, the scaling limit of bilayer BP FET is investigated. It is shown that, while the scaling of gate dielectric monotonically enhances the overall performance of bilayer BP FETs, channel length can only be scaled down to ~8 nm due to significant short-channel effects. Bilayer phosphorene FETs are benchmarked against bilayer MoS$_2$ and WSe$_2$ FETs along with a monolayer phosphorene device, which reveals that bilayer phosphorene FETs have favorable switching characteristics over other similar 2D bilayer semiconductor devices, making both monolayer and bilayer phosphorene attractive for future switching applications.

In general, thickness or the number of layers in 2D semiconductors is a key parameter to determine the material's electronic properties and the overall device performance of 2D material electronics. Therefore, the impact of having different number of phosphorene layers on the transistor performance is investigated next, considering two specific target applications of high-performance and low-power devices. Our results suggest that, for high-performance applications, monolayer phosphorene should be utilized in conventional FET structure since it can provide the equally large on current as other multilayer phosphorenes (I_{on} > 1 mA/μm) without showing a penalty of relatively lower density of states, along with favorableness for steep switching and large immunity to gate-induced drain leakage. On the other hand, more comprehensive approach is required for investigating low-power devices, where operating voltage, doping concentration, and channel length should be carefully engineered along with the thickness of phosphorene in the tunnel FET (TFET) structure to achieve ultra-low leakage current without sacrificing on current significantly. Our extensive simulation results

revealed that either bilayer or trilayer phosphorene can provide the best performance in TFETs with the maximum I_{on}/I_{off} of ~2×10^{11} and the subthreshold swing as low as 13 mV/dec. In addition, our comparative study of phosphorene-based conventional FET and TFET clearly shows the feasibility and the limitation of each device for different target applications, providing irreplaceable insights into the design strategy of phosphorene FETs that can be also extended to other similar layered material electronic devices.

Acknowledgements

Table of Contents

List of Figures

x

List of Tables

Chapter 1 Introduction

1.1 Two-Dimensional Materials

For the last decade, graphene has attracted huge attention from various academic fields [1], [2]. The first demonstrated graphene was achieved by mechanical exfoliation from graphite by using a sticky tape [1]. The quality of graphene obtained by this method is good although it suffers from the limited sample size and low yield. Massive graphene can be achieved by reduction of graphite oxide [3]. Nowadays, chemical vapor deposition (CVD) method is widely used to obtain high-quality and large-scale graphene [4].

Graphene shows extremely high mobility, which can exceed 40000 cm^2 V^{-1} s^{-1} [5]. And also has high thermal conductivity [6]. These suggest the great potential of graphene in next-generation electronic devices and other applications. However, graphene suffers from zero bandgap, which means the I_{on}/I_{off} is significantly limited. The zero bandgap nature results from the cone-shape valence and conduction band structure, where the conduction band bottom meets valance band top at K point. The six Dirac-cones are shown in Figure 1.1(a). The band structure of graphene is shown in Figure 1.1(b), which also shows the zero bandgap at K point. The near linear dispersion relation leads to extremely high carrier mobility.
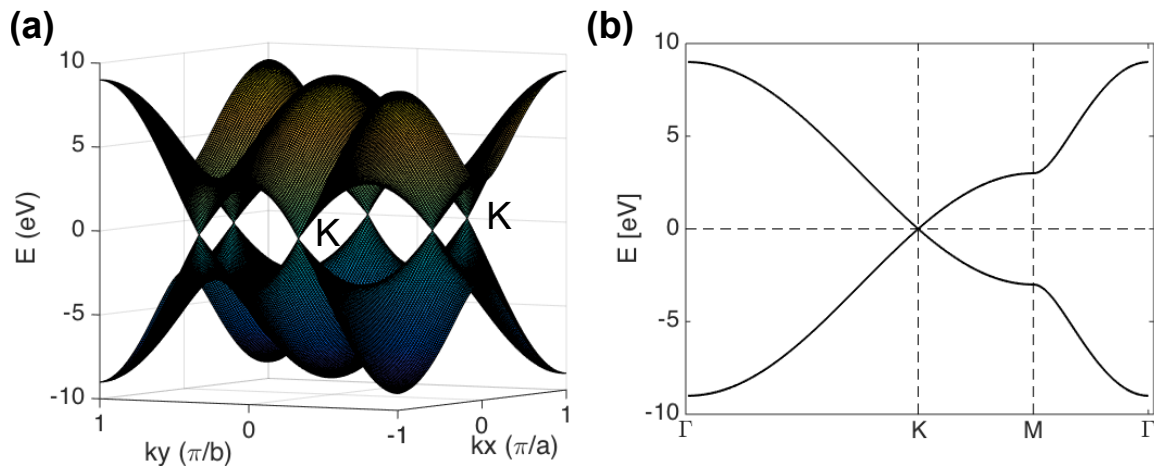
Figure 1.1 (a) 3D band structure of graphene. (b) Band structure of graphene from Γ point to K point to M point and back to Γ point.

There are several ways to obtain a bandgap in graphene: (1) To cut graphene into armchair-edge nanoribbons of chirality of 3N or (3N+1) with width below 10 nm (N is the number of atoms in width direction in GNR). The zigzag-edge graphene nanoribbon (GNR) is metallic and the (3N+2) group

armchair-edge GNR is half-metallic [7], [8]. In practice, it is difficult to control the width and the orientation of GNR accurately, and disorders on edges always exist. The other drawback of this method is the significantly degraded mobility down to only around several hundreds $cm^2 V^{-1} s^{-1}$; (2) To apply strong vertical electric filed across multilayer graphene [9], [10]. However, it requires electric field as high as $1 \sim 3 \times 10^7 V cm^{-1}$ to open a small bandgap around 0.2 eV; (3) To apply strains in graphene [11]–[13]. The bandgap opened by this method is also very small. Because of the limitation of zero bandgap of graphene, new 2D materials with a reasonable bandgap and good mobility are highly desired.

Recently, novel FETs based on layered black phosphorus (BP) have been demonstrated [14]–[16], drawing significant attention in the electronic devices community. Bulk black phosphorus is a layered material like graphite or bulk MoS_2, and currently, thin layers of BP (also called phosphorene) can be obtained by mechanical exfoliation [14], [15], like in the earlier stages of other 2D materials. Silicon-based complementary metal-oxide-semiconductor (CMOS) technology has been standard in modern semiconductor industry for the past decades without significant contenders to compete. However, as consumer electronics are separated from power cords and become more diversified for various applications such as wearable sensors and health care services, demands for new materials in electronics have been dramatically increased. Two-dimensional (2D) layered semiconductors are a class of novel materials that can provide new functionalities in electronics such as flexibility and transparency due to their inherent thinness along with high carrier mobility [17].

1.2 Black Phosphorus

1.2.1 Crystal Structure

Phosphorus atoms are strongly bonded in-plane like carbon atoms in graphite. The layers formed are weakly bonded through van der Waals forces, which are also similar to graphite. However, unlike graphene, phosphorene is not a perfect 2D material since the phosphorus atoms are arranged in a puckered honeycomb lattice. This difference makes band structure of phosphorene quite different from graphene. It opens bandgap, which is critical to digital device applications. Carbon atoms in graphene are bonded through sp^2 hybridized orbitals, while phosphorus atoms in phosphoren are bonded through sp^3 hybridized orbitals. Figure 1.2 gives the crystal structure of bulk form BP, which is fully relaxed by first-principle simulations. The Brillouin zone path of phosphorene primitive cell is also shown in Fig. 1.2.
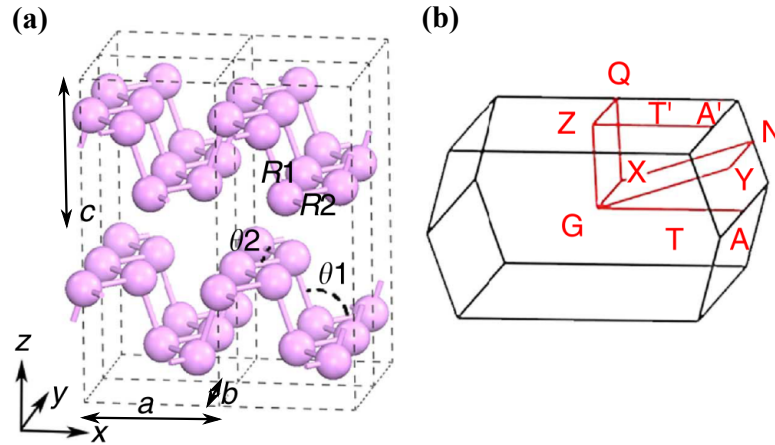
Figure 1.2 (a) Lattice structure of bulk black phosphorus. (b) High symmetric points of bulk BP. In Fig. 1.2(a), the followings are shown: coordinate axes (x, y, z), lattice vectors (a, b, c) and structural parameters (R1, R2) [18]**.**

Since there's no direct experimental data available for the atomic structure of few-layer BP, the atomic structures of few-layer BP are achieved by relaxing structure of bulk form BP [18]. Figure 1.3 shows the atomic structure of few layer BP from top view, its associated Brillouin zone, and the side view of atomic structure of bilayer BP. The structure changes slightly from bulk form to monolayer form. Related structure properties are shown in Table 1.1. The size of unit cell *a* increases abruptly from bilayer to monolayer. The lattice parameter *a,* decreases gently by 0.11Å from bilayer to bulk BP, whereas *b* increases by 0.02 Å. The interlayer spacing is almost constant around 3.20 Å. Like graphene, the honeycomb structure of phosphorene leads to two inequivalent directions, X and Y directions, which are also known as armchair and zigzag directions. Unlike graphene, phosphorene shows strong in-plane anisotropic electrical transport behavior, which means the transport property along X direction is different from Y direction. This will be discussed in details in later chapters.
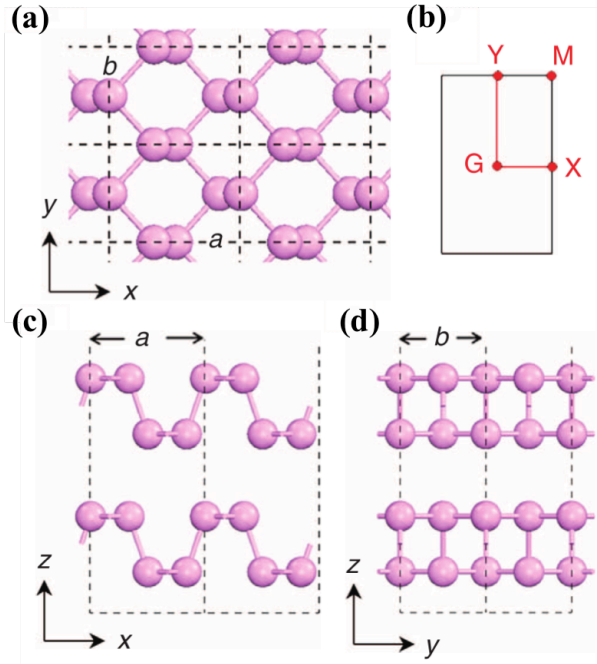
Figure 1.3 (a) Top view of the atomic structure of the monolayer BP. (b) The associated Brillouin zone. (c) (d) Side views of the atomic structure of the bilayer BP [18]**.**

Table 1.1 Structure properties of bulk and few layer BP. *a*, *b* are lattice constant, Δ*c* describes the interlayer spacing between two adjacent BP layers, *θ*1 and *θ*2 are bond angles. There are slight differences in *θ*1 and *θ*2 between the outermost and inner layers [18]**.**

N_L	a(Å)	b(Å)	Δc(Å)	$R1$(Å)	$R2$(Å)	$\theta1/\theta1'$(°)	$\theta2/\theta2'$(°)
1	4.58	3.32	3.20	2.28	2.24	103.51	96.00
2	4.52	3.33	3.20	2.28	2.24	102.96	96.21/95.92
3	4.51	3.33	3.20	2.28	2.24	102.81/102.74	96.30/95.99
4	4.50	3.34	3.20/3.21	2.28	2.24	102.76/102.67	96.34/96.01
5	4.49	3.34	3.20/3.21	2.28	2.24	102.71/102.63	96.37/96.05
Bulk	4.47	3.34	3.20	2.28	2.25	102.42	96.16

1.2.2 Band Structure

One of the unique properties of BP band structure is its dependence on the number of layers, and the bandgap remains direct at Γ point. Figure 1.4 shows the band structure of monolayer, bilayer, trilayer and bulk BP. The light lines are band structures predicted by GW_0 approximation, the dark lines are predicted by tight-binding method adopted in later chapters [19]. The tight-binding method gives a good approximation compared with first-principle method. The theoretically predicted bandgap strongly depends on the applied method, but they commonly exhibit thickness dependence. The bandgap decreases as the number of layer increases. From around 2 eV in its monolayer form, it monotonically decreases to around 0.3 eV for the bulk BP. One can use certain number BP for specific applications. Notably, the 0.3 eV to 2 eV bandgap range cannot be covered by other 2D materials. In this regard, BP can bridge the gap between zero bandgap graphene and larger bandgap transition metal dichalcogenides family. This energy range is especially suitable for thermal imaging, telecom, thermoelectric and photovoltaic applications. BP also provide opportunities in novel flexible and transparent devices where using conventional 3D materials might be challenging [20].
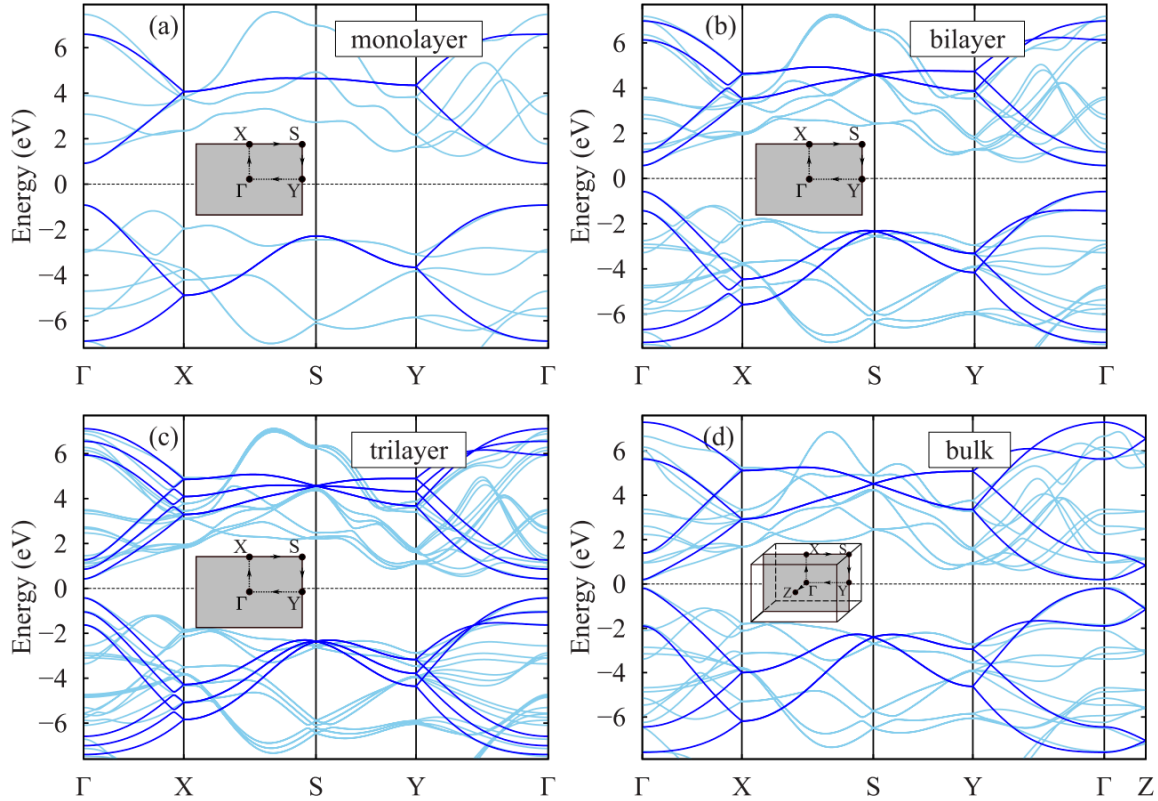
Figure 1.4 Electronic band structures calculated for a few-layer and bulk BP by using the GW_0 approximation (light lines) and within the TB. Fermi level corresponds to the center of the gap. High-symmetry points of the Brillouin zone are shown in the insets [19]**.**

1.2.3 State-of-the-art BP Electronic Devices

It has taken significant less time to get various kinds of nanodevices for BP than for graphene. This is because most of the experiences built up during past decades for graphene devices can be applied to BP directly. Figure 1.5 gives several examples of BP devices with various functionalities. In Figure 1.5(a), the ambipolar field-effect transistor shows a large on-off current ratio (up to 10^5) and high hole mobility (up to 1000 cm^2 V^{-1} s^{-1}) [14]. While most TMDs like MoS_2 and WS_2 are *n*-type, as-grown BP is *p*-type, which is a good complement to build basic components of circuits in CMOS technology. Figure 1.5(b) gives an example of PN junction with electrostatic split-gate geometry [21]. This can be applied to photovoltaic effect in solar cells to separate electron-hold pairs by electric field across PN junctions. Figure 1.5(c) gives a different example in nano-electromechanical applications [22]. The resonance frequency of BP nano-resonator lies in MHz by utilizing the reduced dimensions

and low mass of BP nanosheets. By coupling BP transistors to a silicon waveguide optical resonator, an ultrafast photodetector is fabricated shown in Fig. 1.5(d) [23]. Finally, a potential demonstration of BP in logic circuit application is shown in Fig. 1.5(e) [15]. An inverter amplifier is fabricated by coupling a n-type MoS_2 transistor with p-type BP transistor.
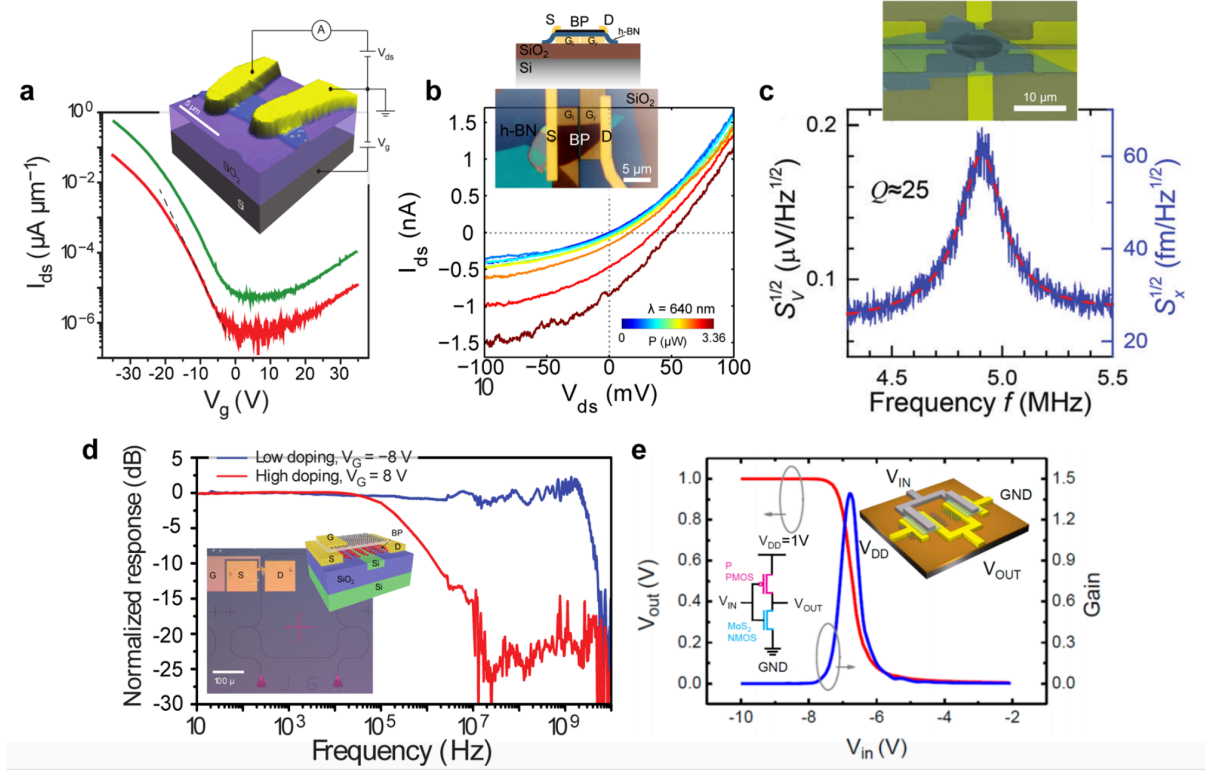
Figure 1.5 Various BP based nanodevices: (a) Ambipolar field-effect transistor (b) Electrostatically gated PN junction displaying photovoltaic effect (c) Nanoelectromechanical resonator vibrating in MHz (d) High frequency photodetector (e) Inverter amplifier based on MoS_2 and black phosphorus transistors [20]**.**

1.3 Simulation Approach

In this thesis, the transport properties of BP FETs are simulated based on the non-equilibrium Green's function (NEGF) formalism with a tight-binding approximation, self-consistently with Poisson's equation [24]. A three terminal device with source, drain and gate is shown in Fig. 1.6. H is the Hamiltonian matrix for the channel region, U describes the self-consistent potential inside the device. Σ_1 and Σ_2 are contact self-energies, describing the electron injection at the channel-contact interfaces. Green's function is calculated for the electron density, which is used in Poisson's equation

to solve electrostatic properties. The calculated potential profile is, in turn, used in NEGF equations to update charge density. These steps will be performed iteratively until a self-consistent result can be achieved.
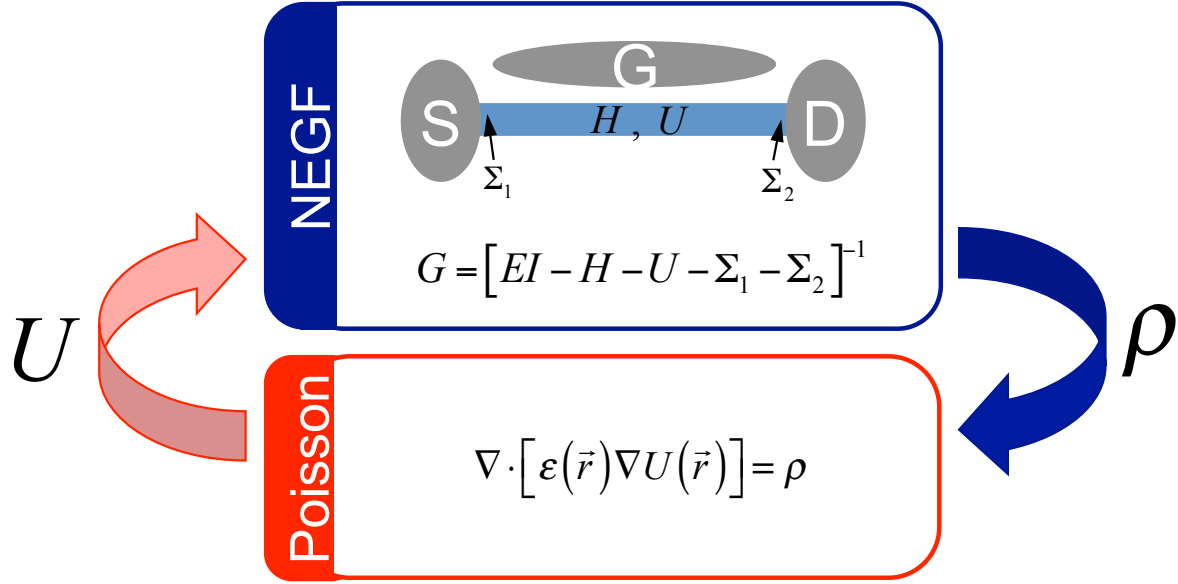
Figure 1.6 Iterative procedure for calculating charge density (ρ) and potential (U) self-consistently.

1.3.1 Non-equilibrium Green's Function Formalism

The retarded Green's function at give energy is

$$G = [EI - H - \Sigma_1 - \Sigma_2]^{-1}.$$

In this equation, H is the Hamiltonian which can be based on effective mass, or $k \cdot p$ or tight-binding method. Self-energy matrices Σ_1 and Σ_2 describe coupling between the channel region and source/drain contacts.

The broadening function is described as $\Gamma_{1,2} = i(\Sigma_{1,2} - \Sigma_{1,2}{}^+)$, which is the anti-Hermitian part of "self-energy" matrix. The spectral function is described as $A(E) = i(G - G^+) = G^n + G^p = A_1 + A_2$. The spectral function [A] represents the matrix version of the density of states per unit energy, and the correlation function [G^n] is the matrix version of the electron density per unit energy. The electron correlation function can be described as $G^n(E) = G(\Gamma_1 f_1 - \Gamma_2 f_2)G^+$. In this equation, f_1 is the source Fermi function and f_2 represents drain Fermi function. The current I_i at terminal i can be

8

written in the form $I_i = (-q/h) \int_{-\infty}^{+\infty} dE \tilde{I}_i(E)$ with $\tilde{I}_i = Trace[\Gamma_i A]f_1 - Trace[\Gamma_i G^n]$. In this way, the current at two terminals is given by

$$I_1 = \frac{q}{h} \int_{-\infty}^{+\infty} dE \, \Gamma_1 \, [A(E)f_1(E) - G^n(E)],$$

$$I_2 = \frac{q}{h} \int_{-\infty}^{+\infty} dE \, \Gamma_2 \, [A(E)f_2(E) - G^n(E)],$$

The transmission can be combined to write

$$\bar{I}_1 = -\bar{I}_2 = \bar{T}(E)\big(f_1(E) - f_2(E)\big),$$

where $\bar{T}(E) = Trace[\Gamma_1 A_2] = Trace[\Gamma_2 A_1]$

The current I in the external circuit is given

$$I = (q/h) \int_{-\infty}^{+\infty} dE \, \bar{T}(E)(f_1(E) - f_2(E)).$$

It should be mentioned that all the simulations performed in this thesis are based on ballistic transport without considering scatterings due to the relatively short channel length.

Chapter 2 Hamiltonian Matrix for Black Phosphorus

2.1 Simplified Parameters

The parameters adopted in this section are tailored exclusively for monolayer and bilayer BP [25]. For multilayer BP, bandgap will be overestimated using these parameters. First, we analyze the crystal structure of BP. There are four atoms in one unit cell, and all the interactions can be include in one unit cell. The unit cell is shown in Figure 2.1 with interactions to neighbor cells. In Figure 2.1 (b) and (c), we give the top view and side view of BP unit cell with numbering of Phosphorus atoms. The order of numbering is import since different numbering can lead to different Hamiltonian matrix. The intralayer and interlayer interactions are shown in Figure 2.2 and the hopping parameters are listed in Table 2.1.
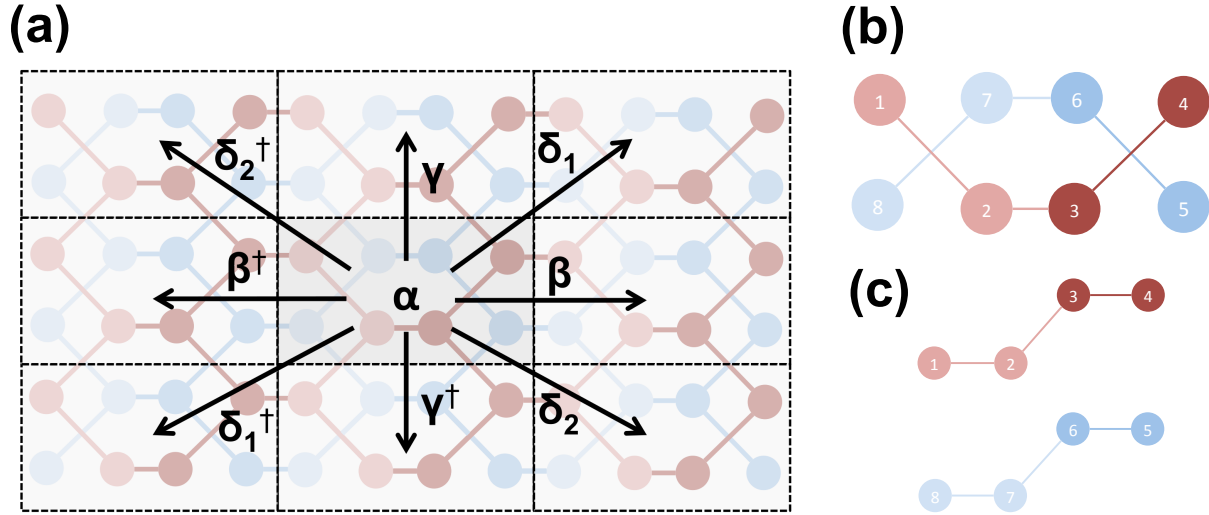
Figure 2.1 (a) Crystal structure of bilayer BP. The dark red layer represents top layer and light blue layer represents bottom layer (b) Top view and (c) Side view of BP unit cell with atom numbering.

Table 2.1 Intralayer (t) and interlayer (h) hopping parameters of tight-binding parameters for monolayer and bilayer BP [25].

	Intralayer (t) (eV)	Interlayer (h) (eV)
1	-1.220	0.295
2	3.665	0.273
3	-0.205	-0.151
4	-0.105	-0.091
5	-0.055	
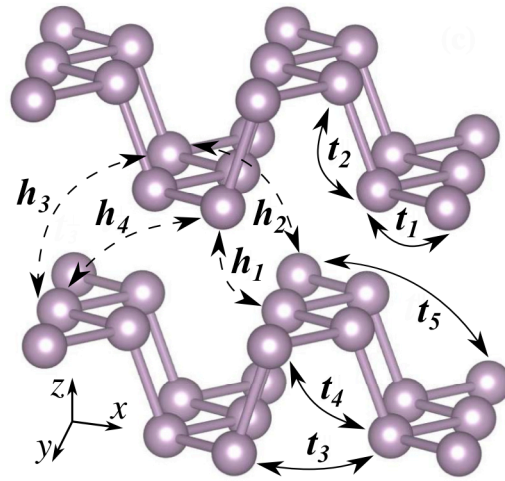
Figure 2.2 Intralayer and interlayer interactions in bilayer BP [25].

2.1.1 Intralayer Interactions in Monolayer BP

We first start from intralayer interactions in monolayer BP. We will use t_1 to t_5 represent intralayer hopping parameters. The Hamiltonian matrix can be written as:

$$\alpha = \begin{bmatrix} 0 & t_1 & t_4 & t_5 \\ t_1 & 0 & t_2 & t_4 \\ t_4 & t_2 & 0 & t_1 \\ t_5 & t_4 & t_1 & 0 \end{bmatrix}$$

$$\beta = \begin{bmatrix} 0 & 0 & 0 & 0 \\ t_3 & 0 & 0 & 0 \\ t_4 & t_5 & 0 & 0 \\ t_2 & t_4 & t_3 & 0 \end{bmatrix}$$

$$\gamma = \begin{bmatrix} 0 & 0 & 0 & 0 \\ t_1 & 0 & 0 & t_4 \\ t_4 & 0 & 0 & t_1 \\ 0 & 0 & 0 & 0 \end{bmatrix}$$

$$\delta_1 = \begin{bmatrix} 0 & 0 & 0 & 0 \\ t_3 & 0 & 0 & 0 \\ t_4 & 0 & 0 & 0 \\ 0 & 0 & 0 & 0 \end{bmatrix}$$

$$\delta_2 = \begin{bmatrix} 0 & 0 & 0 & 0 \\ 0 & 0 & 0 & 0 \\ 0 & 0 & 0 & 0 \\ 0 & t_4 & t_3 & 0 \end{bmatrix}$$

2.1.2 Interlayer Interactions in Bilayer BP

To simplify the way of writing Hamiltonian matrix for bilayer BP, we only need to add the interactions between top layer and bottom layer in monolayer BP Hamiltonian matrix.
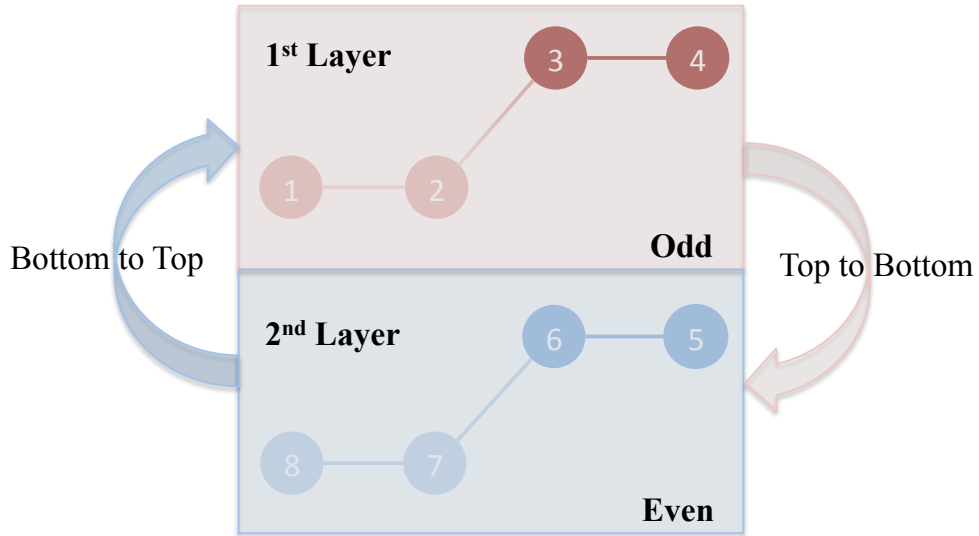
Figure 2.3 Interlayer interactions in bilayer BP unit cell with atom numbering.

The monolayer BP Hamiltonian matrices we got in last section represent the first layer form, which applies to all odd layers. Thus we name them as

$$\alpha_{odd} = \begin{bmatrix} 0 & t_1 & t_4 & t_5 \\ t_1 & 0 & t_2 & t_4 \\ t_4 & t_2 & 0 & t_1 \\ t_5 & t_4 & t_1 & 0 \end{bmatrix}$$

$$\beta_{odd} = \begin{bmatrix} 0 & 0 & 0 & 0 \\ t_3 & 0 & 0 & 0 \\ t_4 & t_5 & 0 & 0 \\ t_2 & t_4 & t_3 & 0 \end{bmatrix}$$

$$\gamma_{odd} = \begin{bmatrix} 0 & 0 & 0 & 0 \\ t_1 & 0 & 0 & t_4 \\ t_4 & 0 & 0 & t_1 \\ 0 & 0 & 0 & 0 \end{bmatrix}$$

$$\delta_{1\,odd} = \begin{bmatrix} 0 & 0 & 0 & 0 \\ t_3 & 0 & 0 & 0 \\ t_4 & 0 & 0 & 0 \\ 0 & 0 & 0 & 0 \end{bmatrix}$$

$$\delta_{2\,odd} = \begin{bmatrix} 0 & 0 & 0 & 0 \\ 0 & 0 & 0 & 0 \\ 0 & 0 & 0 & 0 \\ 0 & t_4 & t_3 & 0 \end{bmatrix}$$

For all even layer BP, the Hamiltonian matrices can be written as:

$$\alpha_{even} = {\alpha_{odd}}^\dagger$$

$$\beta_{even} = {\beta_{odd}}^\dagger$$

$$\gamma_{even} = {\gamma_{odd}}^\dagger$$

$$\delta_{1\,even} = {\delta_{1\,odd}}^\dagger$$

$$\delta_{2\,even} = {\delta_{2\,odd}}^\dagger$$

If we number the top layer as the 1st layer and the bottom layer as the 2nd layer, the interactions from to layer to bottom layer are described in Hamiltonian matrix with subscript *T2B*, the interactions from bottom layer to top layer are described in Hamiltonian matrix with subscript *B2T*.

$$\alpha_{T2B} = \begin{bmatrix} h_4 & h_2 & 0 & 0 \\ h_2 & h_1 & 0 & 0 \\ 0 & 0 & 0 & 0 \\ 0 & 0 & 0 & 0 \end{bmatrix}, \alpha_{B2T} = \begin{bmatrix} h_4 & h_2 & 0 & 0 \\ h_2 & h_1 & 0 & 0 \\ 0 & 0 & 0 & 0 \\ 0 & 0 & 0 & 0 \end{bmatrix}$$

$$\beta_{T2B} = \begin{bmatrix} 0 & 0 & 0 & 0 \\ 0 & 0 & 0 & 0 \\ 0 & 0 & 0 & 0 \\ 0 & 0 & 0 & 0 \end{bmatrix}, \beta_{B2T} = \begin{bmatrix} h_1 & h_2 & 0 & 0 \\ h_2 & h_4 & 0 & 0 \\ 0 & 0 & 0 & 0 \\ 0 & 0 & 0 & 0 \end{bmatrix}$$

$$\gamma_{T2B} = \begin{bmatrix} h_4 & h_3 & 0 & 0 \\ h_3 & 0 & 0 & 0 \\ 0 & 0 & 0 & 0 \\ 0 & 0 & 0 & 0 \end{bmatrix}, \gamma_{B2T} = \begin{bmatrix} 0 & h_3 & 0 & 0 \\ h_3 & h_1 & 0 & 0 \\ 0 & 0 & 0 & 0 \\ 0 & 0 & 0 & 0 \end{bmatrix}$$

$$\delta_{1\,T2B} = \begin{bmatrix} 0 & 0 & 0 & 0 \\ 0 & 0 & 0 & 0 \\ 0 & 0 & 0 & 0 \\ 0 & 0 & 0 & 0 \end{bmatrix}, \delta_{1\,B2T} = \begin{bmatrix} 0 & h_3 & 0 & 0 \\ h_3 & h_4 & 0 & 0 \\ 0 & 0 & 0 & 0 \\ 0 & 0 & 0 & 0 \end{bmatrix}$$

$$\delta_{2\,T2B} = \begin{bmatrix} 0 & 0 & 0 & 0 \\ 0 & 0 & 0 & 0 \\ 0 & 0 & 0 & 0 \\ 0 & 0 & 0 & 0 \end{bmatrix}, \delta_{2\,B2T} = \begin{bmatrix} h_1 & h_3 & 0 & 0 \\ h_3 & 0 & 0 & 0 \\ 0 & 0 & 0 & 0 \\ 0 & 0 & 0 & 0 \end{bmatrix}$$

For the bilayer BP, the final 8 by 8 Hamiltonian matrix can be described as

$$\alpha = \begin{bmatrix} \alpha_{odd} & \alpha_{T2B} \\ \alpha_{B2T} & \alpha_{even} \end{bmatrix}$$

$$\beta = \begin{bmatrix} \beta_{odd} & \beta_{T2B} \\ \beta_{B2T} & \beta_{even} \end{bmatrix}$$

$$\gamma = \begin{bmatrix} \gamma_{odd} & \gamma_{T2B} \\ \gamma_{B2T} & \gamma_{even} \end{bmatrix}$$

$$\delta_1 = \begin{bmatrix} \delta_{1\,odd} & \delta_{1\,T2B} \\ \delta_{1\,B2T} & \delta_{1\,even} \end{bmatrix}$$

$$\delta_2 = \begin{bmatrix} \delta_{2\,odd} & \delta_{2\,T2B} \\ \delta_{2\,B2T} & \delta_{2\,even} \end{bmatrix}$$

2.1.3 Interlayer Interactions in Multilayer BP

Even though the simplified parameters can't predict multilayer BP band structure, the method adopted here is helpful to understand the tight-binding method. And we are using the similar method to get Hamiltonian matrix by advanced tight binding parameters. The simplest multilayer form BP is trilayer BP. The unit cell structure combined with atom numbering is shown in Figure 2.4. Similarly, we use dark red color to represent top layer. The next layer is shown by light blue color.
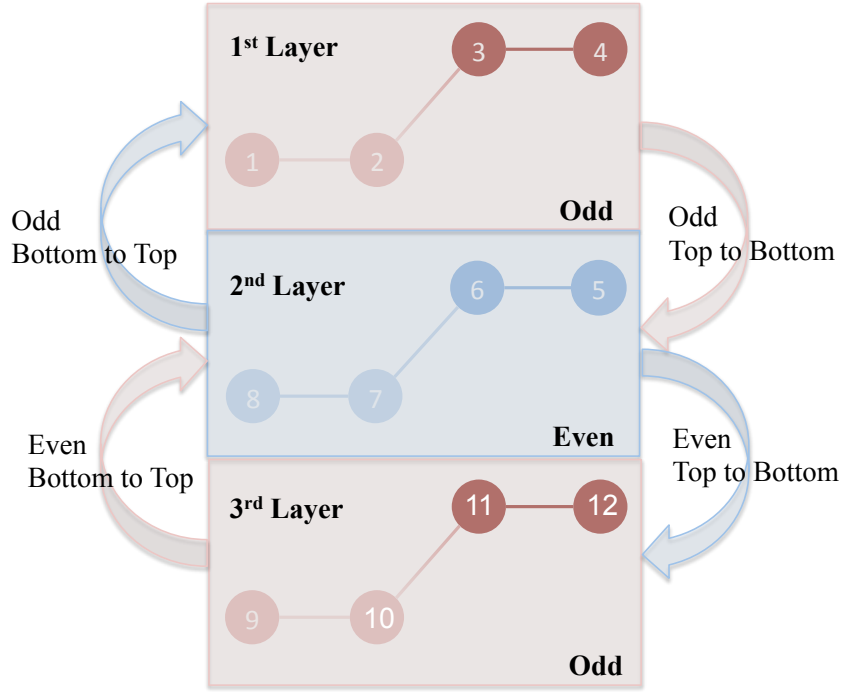
Figure 2.4 Interlayer interactions in trilayer BP unit cell with atom numbering.

The interactions from 1ˢᵗ layer to 2ⁿᵈ layer can also be used to describe interactions from odd layer to even layer. In order to have a naming convention for unity, we name the interaction from 2ⁿᵈ layer to 1ˢᵗ layer as *odd layer bottom to top*, similar for the rest. In this way, we will rename these interlayer interactions as

$$
\alpha_{odd\,T2B} = \begin{bmatrix} h_4 & h_2 & 0 & 0 \\ h_2 & h_1 & 0 & 0 \\ 0 & 0 & 0 & 0 \\ 0 & 0 & 0 & 0 \end{bmatrix}, \qquad
\alpha_{odd\,B2T} = \begin{bmatrix} h_4 & h_2 & 0 & 0 \\ h_2 & h_1 & 0 & 0 \\ 0 & 0 & 0 & 0 \\ 0 & 0 & 0 & 0 \end{bmatrix}
$$

$$
\beta_{odd\,T2B} = \begin{bmatrix} 0 & 0 & 0 & 0 \\ 0 & 0 & 0 & 0 \\ 0 & 0 & 0 & 0 \\ 0 & 0 & 0 & 0 \end{bmatrix}, \qquad
\beta_{odd\,B2T} = \begin{bmatrix} h_1 & h_2 & 0 & 0 \\ h_2 & h_4 & 0 & 0 \\ 0 & 0 & 0 & 0 \\ 0 & 0 & 0 & 0 \end{bmatrix}
$$

$$
\gamma_{odd\,T2B} = \begin{bmatrix} h_4 & h_3 & 0 & 0 \\ h_3 & 0 & 0 & 0 \\ 0 & 0 & 0 & 0 \\ 0 & 0 & 0 & 0 \end{bmatrix}, \qquad
\gamma_{odd\,B2T} = \begin{bmatrix} 0 & h_3 & 0 & 0 \\ h_3 & h_1 & 0 & 0 \\ 0 & 0 & 0 & 0 \\ 0 & 0 & 0 & 0 \end{bmatrix}
$$

$$\delta_{1\,odd\,T2B} = \begin{bmatrix} 0 & 0 & 0 & 0 \\ 0 & 0 & 0 & 0 \\ 0 & 0 & 0 & 0 \\ 0 & 0 & 0 & 0 \end{bmatrix}, \qquad \delta_{1\,odd\,B2T} = \begin{bmatrix} 0 & h_3 & 0 & 0 \\ h_3 & h_4 & 0 & 0 \\ 0 & 0 & 0 & 0 \\ 0 & 0 & 0 & 0 \end{bmatrix}$$

$$\delta_{2\,odd\,T2B} = \begin{bmatrix} 0 & 0 & 0 & 0 \\ 0 & 0 & 0 & 0 \\ 0 & 0 & 0 & 0 \\ 0 & 0 & 0 & 0 \end{bmatrix}, \qquad \delta_{2\,odd\,B2T} = \begin{bmatrix} h_1 & h_3 & 0 & 0 \\ h_3 & 0 & 0 & 0 \\ 0 & 0 & 0 & 0 \\ 0 & 0 & 0 & 0 \end{bmatrix}$$

Similarly, the interactions from 2nd layer to 3rd layer can be classified into interactions between even layer and odd layer. In this way, the numbering should be changed accordingly to convert to bilayer system. The converted unit cell structure is shown in Figure 2.5. Since in this unit cell structure, the top layer is even numbered layer, it is light blue colored. The bottom layer is odd numbered layer and dark red colored.

Figure 2.5 Interlayer interactions in reduced trilayer BP unit cell for interactions between second layer and third layer, and with atom numbering.

The Hamiltonian matrices describing interlayer interactions between second layer and third layer can be written as:

$$\alpha_{even\,T2B} = \begin{bmatrix} 0 & 0 & 0 & 0 \\ 0 & 0 & 0 & 0 \\ 0 & 0 & h_1 & h_2 \\ 0 & 0 & h_2 & h_4 \end{bmatrix}, \qquad \alpha_{even\,B2T} = \begin{bmatrix} 0 & 0 & 0 & 0 \\ 0 & 0 & 0 & 0 \\ 0 & 0 & h_1 & h_2 \\ 0 & 0 & h_2 & h_4 \end{bmatrix}$$

$$\beta_{even\,T2B} = \begin{bmatrix} 0 & 0 & 0 & 0 \\ 0 & 0 & 0 & 0 \\ 0 & 0 & 0 & 0 \\ 0 & 0 & 0 & 0 \end{bmatrix}, \qquad \beta_{even\,B2T} = \begin{bmatrix} 0 & 0 & 0 & 0 \\ 0 & 0 & 0 & 0 \\ 0 & 0 & h_4 & h_2 \\ 0 & 0 & h_2 & h_1 \end{bmatrix}$$

$$\gamma_{even\,T2B} = \begin{bmatrix} 0 & 0 & 0 & 0 \\ 0 & 0 & 0 & 0 \\ 0 & 0 & 0 & h_3 \\ 0 & 0 & h_3 & h_1 \end{bmatrix}, \qquad \gamma_{even\,B2T} = \begin{bmatrix} 0 & 0 & 0 & 0 \\ 0 & 0 & 0 & 0 \\ 0 & 0 & 0 & h_3 \\ 0 & 0 & h_3 & h_4 \end{bmatrix}$$

$$\delta_{1\,even\,T2B} = \begin{bmatrix} 0 & 0 & 0 & 0 \\ 0 & 0 & 0 & 0 \\ 0 & 0 & 0 & 0 \\ 0 & 0 & 0 & 0 \end{bmatrix}, \qquad \delta_{1\,even\,B2T} = \begin{bmatrix} 0 & 0 & 0 & 0 \\ 0 & 0 & 0 & 0 \\ 0 & 0 & 0 & h_3 \\ 0 & 0 & h_3 & h_1 \end{bmatrix}$$

$$\delta_{2\,even\,T2B} = \begin{bmatrix} 0 & 0 & 0 & 0 \\ 0 & 0 & 0 & 0 \\ 0 & 0 & 0 & 0 \\ 0 & 0 & 0 & 0 \end{bmatrix}, \qquad \delta_{2\,even\,B2T} = \begin{bmatrix} 0 & 0 & 0 & 0 \\ 0 & 0 & 0 & 0 \\ 0 & 0 & h_4 & h_3 \\ 0 & 0 & h_3 & 0 \end{bmatrix}$$

Since we have got the Hamiltonian matrices for odd and even layer BP describing intralayer interactions, and also Hamiltonian matrices describing interlayer interactions between odd and even layers. The trilayer BP Hamiltonian matrices can be written as:

$$\alpha = \begin{bmatrix} \alpha_{odd} & \alpha_{odd\,T2B} & 0 \\ \alpha_{odd\,B2T} & \alpha_{even} & \alpha_{even\,T2B} \\ 0 & \alpha_{even\,B2T} & \alpha_{odd} \end{bmatrix}$$

$$\beta = \begin{bmatrix} \beta_{odd} & \beta_{odd\,T2B} & 0 \\ \beta_{odd\,B2T} & \beta_{even} & \beta_{even\,T2B} \\ 0 & \beta_{even\,B2T} & \beta_{odd} \end{bmatrix}$$

$$\gamma = \begin{bmatrix} \gamma_{odd} & \gamma_{odd\,T2B} & 0 \\ \gamma_{odd\,BT2} & \gamma_{even} & \gamma_{even\,T2B} \\ 0 & \gamma_{even\,B2T} & \gamma_{odd} \end{bmatrix}$$

$$\delta_1 = \begin{bmatrix} \delta_{1\,odd} & \delta_{1\,odd\,T2B} & 0 \\ \delta_{1\,odd\,B2T} & \delta_{1\,even} & \delta_{1\,even\,T2B} \\ 0 & \delta_{1\,even\,B2T} & \delta_{1\,odd} \end{bmatrix}$$

$$\delta_2 = \begin{bmatrix} \delta_{2\,odd} & \delta_{2\,odd\,T2B} & 0 \\ \delta_{2\,odd\,B2T} & \delta_{2\,even} & \delta_{2\,even\,T2B} \\ 0 & \delta_{2\,even\,B2T} & \delta_{2\,odd} \end{bmatrix}$$

For multilayer BP, we can just add matrix in the diagonal and the upper and lower diagonal elements accordingly. If we know the Hamiltonian matrix of n layer BP as $\alpha_n, \beta_n, \gamma_n, \delta_{1_n}, \delta_{2_n}$, if the nth layer is odd layer, the Hamiltonian matrix of $n+1$ layer BP would be:

$$\alpha_{n+1} = \begin{bmatrix} \alpha_n & \alpha_{odd\,T2B} \\ \alpha_{odd\,B2T} & \alpha_{even} \end{bmatrix}$$

$$\beta_{n+1} = \begin{bmatrix} \beta_n & \beta_{odd\,T2B} \\ \beta_{odd\,B2T} & \beta_{even} \end{bmatrix},$$

$$\gamma_{n+1} = \begin{bmatrix} \gamma_n & \gamma_{odd\,T2B} \\ \gamma_{odd\,B2T} & \gamma_{even} \end{bmatrix},$$

$$\delta_{1n+1} = \begin{bmatrix} \delta_{1n} & \delta_{1\,odd\,T2B} \\ \delta_{1\,odd\,B2T} & \delta_{1\,even} \end{bmatrix},$$

$$\delta_{2n+1} = \begin{bmatrix} \delta_{2n} & \delta_{2\,odd\,T2B} \\ \delta_{2\,odd\,B2T} & \delta_{2\,even} \end{bmatrix}$$

If the nth layer is even layer, the Hamiltonian matrix of $n+1$ layer BP would be:

$$\alpha_{n+1} = \begin{bmatrix} \alpha_n & \alpha_{even\,T2B} \\ \alpha_{even\,B2T} & \alpha_{odd} \end{bmatrix}$$

$$\beta_{n+1} = \begin{bmatrix} \beta_n & \beta_{evne\,T2B} \\ \beta_{even\,B2T} & \beta_{odd} \end{bmatrix},$$

$$\gamma_{n+1} = \begin{bmatrix} \gamma_n & \gamma_{even\,T2B} \\ \gamma_{even\,B2T} & \gamma_{odd} \end{bmatrix},$$

$$\delta_{1n+1} = \begin{bmatrix} \delta_{1n} & \delta_{1\,even\,T2B} \\ \delta_{1\,even\,B2T} & \delta_{1\,odd} \end{bmatrix},$$

$$\delta_{2n+1} = \begin{bmatrix} \delta_{2n} & \delta_{2\,even\,T2B} \\ \delta_{2\,even\,B2T} & \delta_{2\,odd} \end{bmatrix}$$

2.2 Advanced Parameters

The parameters adopted in this section are tailored for multilayer BP. It can give good predictions on band gap from monolayer up to bulk form BP. Since the intralayer interaction t_8 can not be included in one unit cell. A supercell structure is used for advanced tight binding parameters. The structure of supercell is shown in Figure 2.6 with neighboring supercells. Figure 2.6 (b) and (c) give the top view and side view of supercell and the corresponding numbering. The hopping parameters are listed in Table 2.2. And the intralayer and interlayer interactions are shown in Figure 2.7.
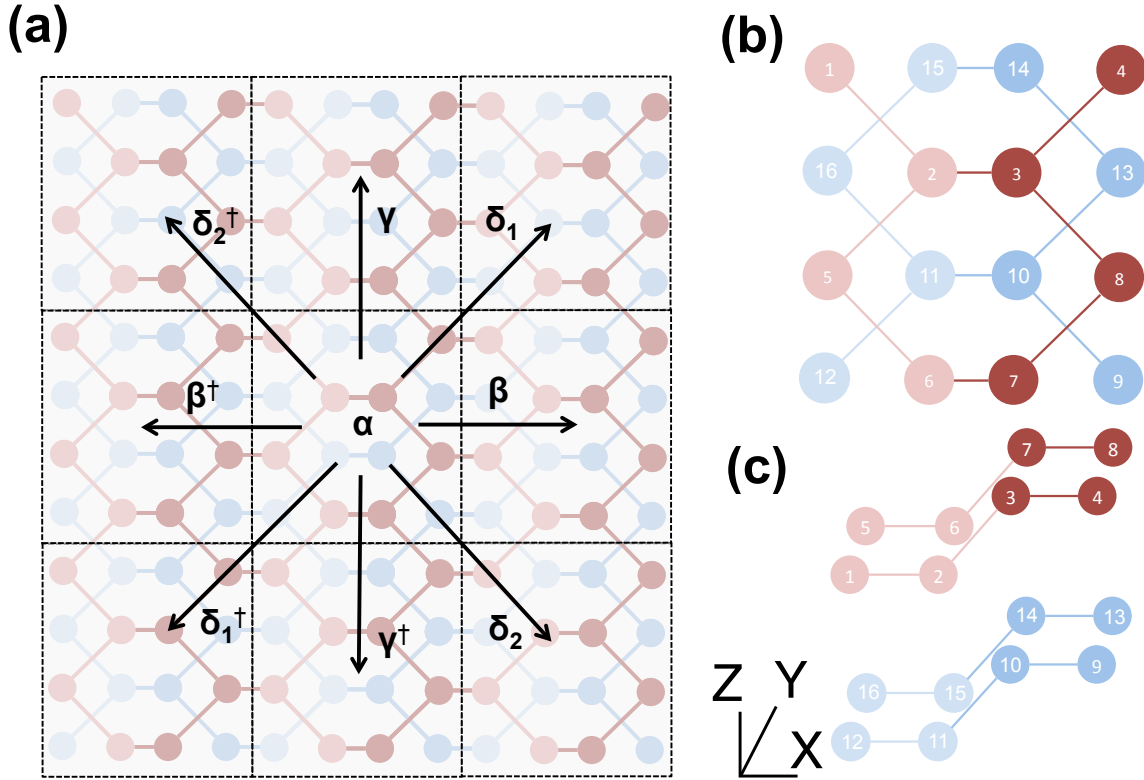
Figure 2.6 (a) Crystal structure of bilayer BP using supercell. The dark red layer represents top layer and light blue layer represents bottom layer (b) Top view and (c) Side view of BP supercell with atom numbering. The x, y and z axes are following Figure 1.3.

Table 2.2 Intralayer (t) and interlayer (h) hopping parameters of tight-binding parameters for multilayer BP [19].

	Intralayer (t) (eV)			Interlayer (h) (eV)	
1	-1.486	**6**	+0.186	**1**	+0.524
2	3.729	**7**	-0.063	**2**	+0.180
3	-0.252	**8**	+0.101	**3**	-0.123
4	-0.071	**9**	-0.042	**4**	-0.168
5	+0.019	**10**	+0.073	**5**	+0.005
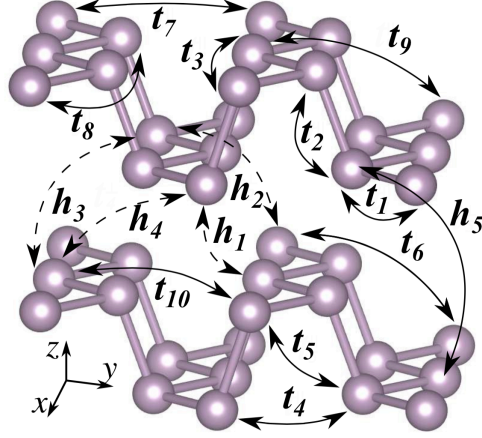
Figure 2.7 Intralayer and interlayer interactions in bilayer BP using advanced tight-binding parameters [19]**.**

2.2.1 Intralayer Interactions in Monolayer BP

To simplify Hamiltonian matrix, the 8 by 8 matrices are decomposed into four 4 by 4 matrices

$$\alpha_{11} = \begin{bmatrix} 0 & t_1 & t_5 & t_6 \\ t_1 & 0 & t_2 & t_5 \\ t_5 & t_2 & 0 & t_1 \\ t_6 & t_5 & t_1 & 0 \end{bmatrix}, \alpha_{12} = \begin{bmatrix} t_3 & t_8 & 0 & t_9 \\ t_1 & t_3 & 0 & t_5 \\ t_5 & 0 & t_3 & t_1 \\ t_9 & 0 & t_8 & t_3 \end{bmatrix}, \alpha_{21} = {\alpha_{12}}^{\dagger}, \alpha_{22} = {\alpha_{11}}^{\dagger}$$

$$\beta_{11} = \beta_{22} = \begin{bmatrix} t_7 & 0 & 0 & 0 \\ t_4 & t_7 & 0 & 0 \\ t_5 & t_6 & t_7 & 0 \\ t_2 & t_5 & t_4 & t_7 \end{bmatrix}, \beta_{12} = \begin{bmatrix} t_{10} & 0 & 0 & 0 \\ t_4 & t_{10} & 0 & 0 \\ t_5 & t_9 & t_{10} & 0 \\ 0 & 0 & 0 & t_{10} \end{bmatrix}, \beta_{21} = \begin{bmatrix} t_{10} & 0 & 0 & 0 \\ 0 & t_{10} & 0 & 0 \\ 0 & t_9 & t_{10} & 0 \\ 0 & t_5 & t_4 & t_{10} \end{bmatrix}$$

$$\gamma_{11} = \gamma_{22} = \begin{bmatrix} 0 & t_8 & 0 & 0 \\ 0 & 0 & 0 & 0 \\ 0 & 0 & 0 & 0 \\ 0 & 0 & t_8 & 0 \end{bmatrix}, \gamma_{12} = \begin{bmatrix} t_3 & t_1 & t_5 & t_9 \\ t_8 & t_3 & 0 & 0 \\ 0 & 0 & t_3 & t_8 \\ t_9 & t_5 & t_1 & t_3 \end{bmatrix}, \gamma_{21} = \begin{bmatrix} 0 & 0 & 0 & 0 \\ 0 & 0 & 0 & 0 \\ 0 & 0 & 0 & 0 \\ 0 & 0 & 0 & 0 \end{bmatrix}$$

$$\delta_{1_{11}} = \delta_{1_{21}} = \delta_{1_{22}} = \begin{bmatrix} 0 & 0 & 0 & 0 \\ 0 & 0 & 0 & 0 \\ 0 & 0 & 0 & 0 \\ 0 & 0 & 0 & 0 \end{bmatrix}, \delta_{1_{21}} = \begin{bmatrix} t_{10} & 0 & 0 & 0 \\ 0 & t_{10} & 0 & 0 \\ 0 & t_9 & t_{10} & 0 \\ 0 & t_5 & t_4 & t_{10} \end{bmatrix}$$

$$\delta_{2_{11}} = \delta_{2_{12}} = \delta_{2_{22}} = \begin{bmatrix} 0 & 0 & 0 & 0 \\ 0 & 0 & 0 & 0 \\ 0 & 0 & 0 & 0 \\ 0 & 0 & 0 & 0 \end{bmatrix}, \delta_{2_{21}} = \begin{bmatrix} t_{10} & 0 & 0 & 0 \\ t_4 & t_{10} & 0 & 0 \\ t_5 & t_9 & t_{10} & 0 \\ 0 & 0 & 0 & t_{10} \end{bmatrix}$$

As there are also even and odd layers, the odd layers (which consists 1st, 3rd, 5th and so on) intralayer interactions can be expressed as

$$\alpha_{odd} = \begin{bmatrix} \alpha_{11} & \alpha_{12} \\ \alpha_{21} & \alpha_{22} \end{bmatrix}$$

$$\beta_{odd} = \begin{bmatrix} \beta_{11} & \beta_{12} \\ \beta_{21} & \beta_{22} \end{bmatrix}$$

$$\gamma_{odd} = \begin{bmatrix} \gamma_{11} & \gamma_{12} \\ \gamma_{21} & \gamma_{22} \end{bmatrix}$$

$$\delta_{1odd} = \begin{bmatrix} \delta_{111} & \delta_{112} \\ \delta_{121} & \delta_{122} \end{bmatrix}$$

$$\delta_{2odd} = \begin{bmatrix} \delta_{211} & \delta_{212} \\ \delta_{221} & \delta_{222} \end{bmatrix}$$

The even layer intralayer interactions can be expressed as:

$$\alpha_{even} = \alpha_{odd}{}^{\dagger}, \beta_{even} = \beta_{odd}{}^{\dagger}, \gamma_{even} = \gamma_{odd}{}^{\dagger}, \delta_{1even} = \delta_{1odd}{}^{\dagger}, \delta_{2even} = \delta_{2odd}{}^{\dagger}$$

2.2.2 Interlayer Interactions in Bilayer BP

We will also use four 8 by 8 matrix to represent 16 by 16 Hamiltonian matrix of bilayer form. And we will use similar steps adopted in simplified tight binding matrix method, to get multilayer Hamiltonian matrix. Because of the supercell structure, we can decompose the 8 by 8 matrix into 4 by 4 matrix by using Hamiltonian matrix of unit cell structure. For the unit cell structure, we use the same notations as in previous chapter to represent interlayer interactions. For interactions from odd layer to even layers (1st to 2nd, 3rd to 4th, and so on), we will use α_{oddT2B} to represent interlayer interactions from top layer to bottom layer, α_{oddB2T} to represent interlayer interactions from bottom to top layer, the same for the rest. The Hamiltonian matrices describing odd to even layers are as follows:

$$\alpha_{oddT2B} = \begin{bmatrix} h_4 & h_2 & 0 & 0 \\ h_2 & h_1 & 0 & 0 \\ 0 & 0 & 0 & 0 \\ 0 & 0 & 0 & 0 \end{bmatrix}, \qquad \alpha_{oddB2T} = \begin{bmatrix} h_4 & h_2 & 0 & 0 \\ h_2 & h_1 & 0 & 0 \\ 0 & 0 & 0 & 0 \\ 0 & 0 & 0 & 0 \end{bmatrix}$$
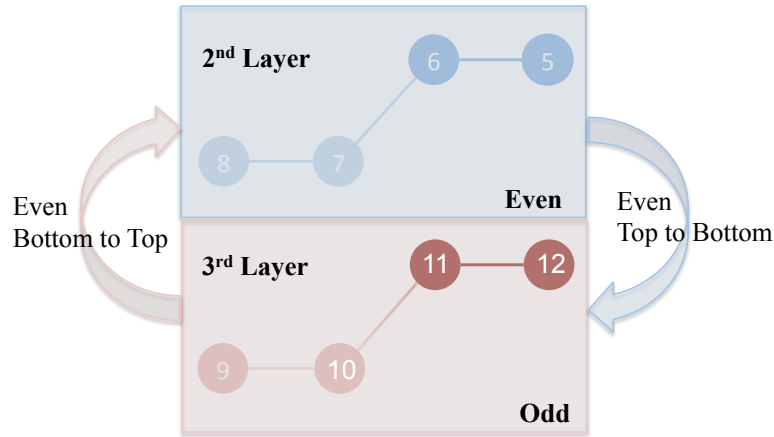
$$\beta_{oddT2B} = \begin{bmatrix} 0 & 0 & 0 & 0 \\ 0 & 0 & 0 & 0 \\ 0 & 0 & 0 & 0 \\ 0 & 0 & 0 & 0 \end{bmatrix}, \qquad \beta_{oddB2T} = \begin{bmatrix} h_1 & h_2 & 0 & 0 \\ h_2 & h_4 & 0 & 0 \\ 0 & 0 & 0 & 0 \\ 0 & 0 & 0 & 0 \end{bmatrix}$$

21

$$\gamma_{odd\,T2B} = \begin{bmatrix} h_4 & h_3 & h_5 & 0 \\ h_3 & 0 & 0 & h_5 \\ 0 & 0 & 0 & 0 \\ 0 & 0 & 0 & 0 \end{bmatrix}, \quad \gamma_{odd\,B2T} = \begin{bmatrix} 0 & h_3 & 0 & 0 \\ h_3 & h_1 & 0 & 0 \\ h_5 & 0 & 0 & 0 \\ 0 & h_5 & 0 & 0 \end{bmatrix}$$

$$\delta_{1\,odd\,T2B} = \begin{bmatrix} 0 & 0 & 0 & 0 \\ 0 & 0 & 0 & 0 \\ 0 & 0 & 0 & 0 \\ 0 & 0 & 0 & 0 \end{bmatrix}, \quad \delta_{1\,odd\,B2T} = \begin{bmatrix} 0 & h_3 & 0 & 0 \\ h_3 & h_4 & 0 & 0 \\ 0 & 0 & 0 & 0 \\ 0 & 0 & 0 & 0 \end{bmatrix}$$

$$\delta_{2\,odd\,T2B} = \begin{bmatrix} 0 & 0 & 0 & 0 \\ 0 & 0 & 0 & 0 \\ 0 & 0 & 0 & 0 \\ 0 & 0 & 0 & 0 \end{bmatrix}, \quad \delta_{2\,odd\,B2T} = \begin{bmatrix} h_1 & h_3 & 0 & 0 \\ h_3 & 0 & 0 & 0 \\ 0 & 0 & 0 & 0 \\ 0 & 0 & 0 & 0 \end{bmatrix}$$

The Hamiltonian matrices describing even to odd layers are as follows:

$$\alpha_{even\,T2B} = \begin{bmatrix} 0 & 0 & 0 & 0 \\ 0 & 0 & 0 & 0 \\ 0 & 0 & h_1 & h_2 \\ 0 & 0 & h_2 & h_4 \end{bmatrix}, \quad \alpha_{even\,B2T} = \begin{bmatrix} 0 & 0 & 0 & 0 \\ 0 & 0 & 0 & 0 \\ 0 & 0 & h_1 & h_2 \\ 0 & 0 & h_2 & h_4 \end{bmatrix}$$

$$\beta_{even\,T2B} = \begin{bmatrix} 0 & 0 & 0 & 0 \\ 0 & 0 & 0 & 0 \\ 0 & 0 & 0 & 0 \\ 0 & 0 & 0 & 0 \end{bmatrix}, \quad \beta_{even\,B2T} = \begin{bmatrix} 0 & 0 & 0 & 0 \\ 0 & 0 & 0 & 0 \\ 0 & 0 & h_4 & h_2 \\ 0 & 0 & h_2 & h_1 \end{bmatrix}$$

$$\gamma_{even\,T2B} = \begin{bmatrix} 0 & 0 & 0 & 0 \\ 0 & 0 & 0 & 0 \\ h_5 & 0 & 0 & h_3 \\ 0 & h_5 & h_3 & h_1 \end{bmatrix}, \quad \gamma_{even\,B2T} = \begin{bmatrix} 0 & 0 & h_5 & 0 \\ 0 & 0 & 0 & h_5 \\ 0 & 0 & 0 & h_3 \\ 0 & 0 & h_3 & h_4 \end{bmatrix}$$

$$\delta_{1\,even\,T2B} = \begin{bmatrix} 0 & 0 & 0 & 0 \\ 0 & 0 & 0 & 0 \\ 0 & 0 & 0 & 0 \\ 0 & 0 & 0 & 0 \end{bmatrix}, \quad \delta_{1\,even\,B2T} = \begin{bmatrix} 0 & 0 & 0 & 0 \\ 0 & 0 & 0 & 0 \\ 0 & 0 & 0 & h_3 \\ 0 & 0 & h_3 & h_1 \end{bmatrix}$$

$$\delta_{2\,even\,T2B} = \begin{bmatrix} 0 & 0 & 0 & 0 \\ 0 & 0 & 0 & 0 \\ 0 & 0 & 0 & 0 \\ 0 & 0 & 0 & 0 \end{bmatrix}, \quad \delta_{2\,even\,B2T} = \begin{bmatrix} 0 & 0 & 0 & 0 \\ 0 & 0 & 0 & 0 \\ 0 & 0 & h_4 & h_3 \\ 0 & 0 & h_3 & 0 \end{bmatrix}$$

Now we can use these 4 by 4 matrices to represent the interactions for supercell structure. For interactions from odd layer to even layer, like 1st to 2nd, 3rd to 4th and so on, we will use $\alpha_{ODD\,T2B}$ to represent the interlayer interactions from top to bottom layer, $\alpha_{ODD\,B2T}$ to represent the interlayer

interactions from bottom to top layer, same for the rest. (Capital letters are used here to distinguish from interlayer interactions in unit cell structure.) The Hamiltonian matrices are as following:

$$\alpha_{ODD\,T2B} = \begin{bmatrix} \gamma_{odd\,B2T}{}^\dagger & \alpha_{odd\,T2B} \\ \alpha_{odd\,T2B} & \gamma_{odd\,T2B} \end{bmatrix}, \qquad \alpha_{ODD\,B2T} = \begin{bmatrix} \gamma_{odd\,B2T} & \alpha_{odd\,B2T} \\ \alpha_{odd\,B2T} & \gamma_{odd\,T2B}{}^\dagger \end{bmatrix}$$

$$\beta_{ODD\,T2B} = \begin{bmatrix} \delta_{2\,odd\,T2B} & \beta_{odd\,T2B} \\ \beta_{odd\,T2B} & \delta_{1\,odd\,T2B} \end{bmatrix}, \qquad \beta_{ODD\,B2T} = \begin{bmatrix} \delta_{1\,odd\,B2T} & \beta_{odd\,B2T} \\ \beta_{odd\,B2T} & \delta_{2\,odd\,B2T} \end{bmatrix}$$

$$\gamma_{ODD\,T2B} = \begin{bmatrix} \gamma_{odd\,T2B} & 0 \\ 0 & 0 \end{bmatrix}, \qquad \gamma_{ODD\,B2T} = \begin{bmatrix} 0 & 0 \\ 0 & \gamma_{odd\,B2T} \end{bmatrix}$$

$$\delta_{1\,ODD\,T2B} = \begin{bmatrix} \delta_{1\,odd\,T2B} & 0 \\ 0 & 0 \end{bmatrix}, \qquad \delta_{1\,ODD\,B2T} = \begin{bmatrix} 0 & 0 \\ 0 & \delta_{1\,odd\,B2T} \end{bmatrix}$$

$$\delta_{2\,ODD\,T2B} = \begin{bmatrix} 0 & 0 \\ 0 & \delta_{2\,odd\,T2B} \end{bmatrix}, \qquad \delta_{2\,ODD\,B2T} = \begin{bmatrix} \delta_{2\,odd\,B2T} & 0 \\ 0 & 0 \end{bmatrix}$$

For interactions from even layer to odd layer, like 2nd to 3rd, 4th to 5th and s on, the interlayer interactions are: (Capital letters are used to distinguish from unit cell form)

$$\alpha_{EVEN\,T2B} = \begin{bmatrix} \gamma_{even\,T2B} & \alpha_{even\,T2B} \\ \alpha_{even\,T2B} & \gamma_{even\,B2T}{}^\dagger \end{bmatrix}, \qquad \alpha_{EVEN\,DtoU} = \begin{bmatrix} \gamma_{even\,T2B} & \alpha_{even\,B2T} \\ \alpha_{even\,B2T} & \gamma_{even\,B2T}{}^\dagger \end{bmatrix}$$

$$\beta_{EVEN\,T2B} = \begin{bmatrix} \delta_{2\,even\,B2T} & \beta_{even\,B2T} \\ \beta_{even\,B2T} & \delta_{1\,even\,B2T} \end{bmatrix}, \qquad \beta_{EVEN\,DtoU} = \begin{bmatrix} \delta_{1\,even\,T2B} & \beta_{even\,T2B} \\ \beta_{even\,T2B} & \delta_{2\,even\,T2B} \end{bmatrix}$$

$$\gamma_{EVEN\,T2B} = \begin{bmatrix} 0 & 0 \\ 0 & \gamma_{even\,T2B} \end{bmatrix}, \qquad \gamma_{EVEN\,DtoU} = \begin{bmatrix} \gamma_{even\,B2T} & 0 \\ 0 & 0 \end{bmatrix}$$

$$\delta_{1\,EVEN\,T2B} = \begin{bmatrix} 0 & 0 \\ 0 & \delta_{1\,even\,T2B} \end{bmatrix}, \qquad \delta_{1\,EVEN\,DtoU} = \begin{bmatrix} \delta_{1\,even\,B2T} & 0 \\ 0 & 0 \end{bmatrix}$$

$$\delta_{2\,EVEN\,UtoD} = \begin{bmatrix} \delta_{2\,even\,T2B} & 0 \\ 0 & 0 \end{bmatrix}, \qquad \delta_{2\,EVEN\,DtoU} = \begin{bmatrix} 0 & 0 \\ 0 & \delta_{2\,even\,B2T} \end{bmatrix}$$

Once we have all the interlayer interactions, we can get any multilayer Hamiltonian matrix by using the following method: If the nth layer is odd layer and the $\boldsymbol{\alpha_n}$ represent the Hamiltonian matrix of $\boldsymbol{n}$ layer BP, the Hamiltonian matrix of $\boldsymbol{n+1}$ layer BP would be:

$$\boldsymbol{\alpha_{n+1}} = \begin{bmatrix} \boldsymbol{\alpha_n} & \alpha_{ODD\,T2B} \\ \alpha_{ODD\,B2T} & \alpha_{EVEN} \end{bmatrix}$$

23

$$\boldsymbol{\beta_{n+1}} = \begin{bmatrix} \boldsymbol{\beta_n} & \beta_{ODD\,T2B} \\ \beta_{ODD\,B2T} & \beta_{EVEN} \end{bmatrix},$$

$$\boldsymbol{\gamma_{n+1}} = \begin{bmatrix} \boldsymbol{\gamma_n} & \gamma_{ODD\,T2B} \\ \gamma_{ODD\,B2T} & \gamma_{EVEN} \end{bmatrix},$$

$$\boldsymbol{\delta_{1\,n+1}} = \begin{bmatrix} \boldsymbol{\delta_{1n}} & \delta_{1\,ODD\,T2B} \\ \delta_{1\,ODD\,B2T} & \delta_{1\,EVEN} \end{bmatrix},$$

$$\boldsymbol{\delta_{2\,n+1}} = \begin{bmatrix} \boldsymbol{\delta_{2n}} & \delta_{2\,ODD\,T2B} \\ \delta_{2\,ODD\,B2T} & \delta_{2\,EVEN} \end{bmatrix}$$

If the nth layer is even layer, the Hamiltonian matrix of **$n+1$** layer BP would be:

$$\boldsymbol{\alpha_{n+1}} = \begin{bmatrix} \boldsymbol{\alpha_n} & \alpha_{EVEN\,T2B} \\ \alpha_{EVEN\,B2T} & \alpha_{ODD} \end{bmatrix}$$

$$\boldsymbol{\beta_{n+1}} = \begin{bmatrix} \boldsymbol{\beta_n} & \beta_{EVEN\,T2B} \\ \beta_{EVEN\,B2T} & \beta_{ODD} \end{bmatrix},$$

$$\boldsymbol{\gamma_{n+1}} = \begin{bmatrix} \boldsymbol{\gamma_n} & \gamma_{EVEN\,T2B} \\ \gamma_{EVEN\,B2T} & \gamma_{ODD} \end{bmatrix},$$

$$\boldsymbol{\delta_{1\,n+1}} = \begin{bmatrix} \boldsymbol{\delta_{1n}} & \delta_{1\,EVEN\,T2B} \\ \delta_{1\,EVEN\,B2T} & \delta_{1\,ODD} \end{bmatrix},$$

$$\boldsymbol{\delta_{2\,n+1}} = \begin{bmatrix} \boldsymbol{\delta_{2n}} & \delta_{2\,EVEN\,T2B} \\ \delta_{2\,EVEN\,B2T} & \delta_{2\,ODD} \end{bmatrix}$$

2.3 Zone Folding in Advanced Tight-binding Parameters

Since the simplified tight-binding parameters are tailored for monolayer and bilayer. The band structures calculated are shown in Figure 2.8. The Fermi level is shifted to the mid-bandgap by adding additional element Δt to diagonal elements in $\boldsymbol{\alpha}$ matrix. The bandgap for monolayer and bilayer BP are 1.52 and 1.12 eV respectively. Both monolayer and bilayer BP show direct bandgap and the minimum bandgap lies in Γ point.

The band structures predicted by advance parameters are shown in Figure 2.9. From (a) to (d), band structures of monolayer to tetralayer BP are shown. The bandgaps are 1.84, 1.15, 0.85 and 0.70 eV respectively. They all show direct bandgap and minmum bandgap lies in Γ point.
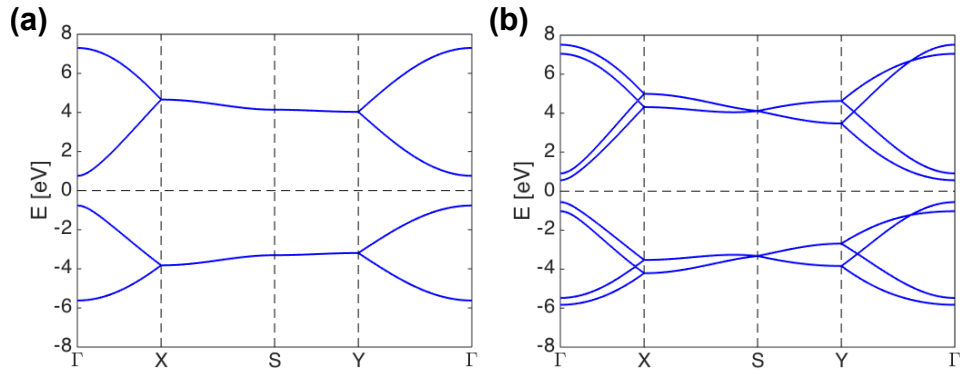
Figure 2.8 (a) Monolayer and (b) Bilayer band structure calculated by simplified tight-binding parameters.
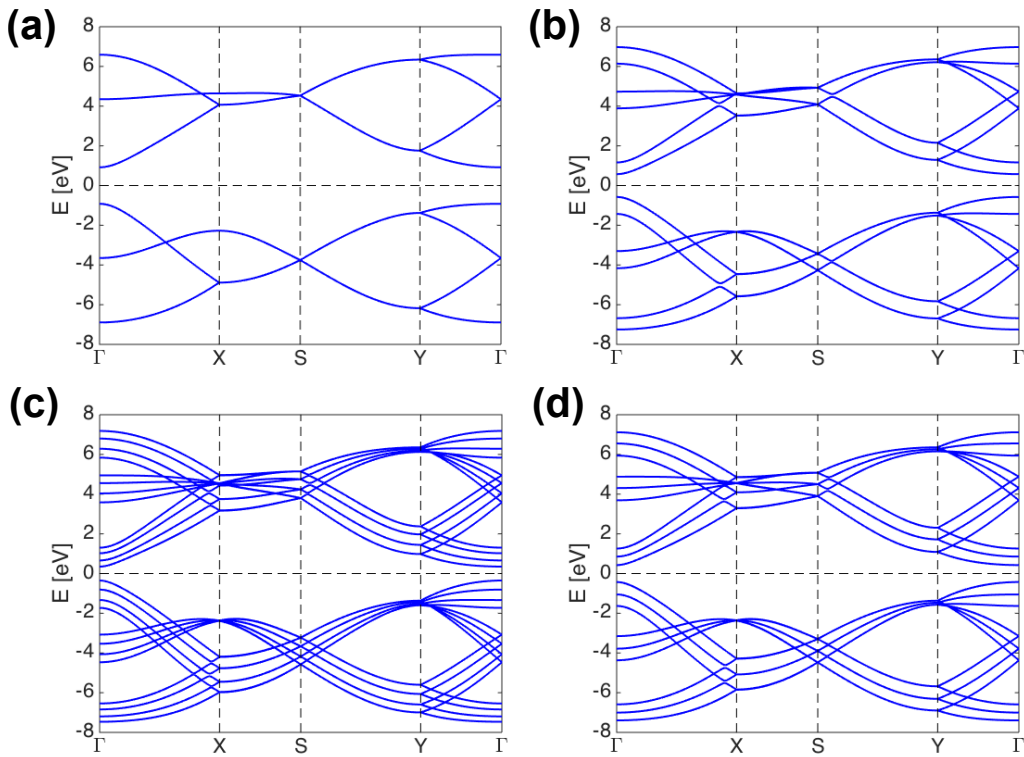
Figure 2.9 (a) Monolayer and (b) Bilayer (c) Trilayer (d) Tetralayer BP band structure calculated by advanced tight-binding parameters.

We notice band folding in band structures predicted by advanced tight-binding parameters. This is because the supercell structure is adopted. The real space supercell is doubled, thus the k space is half

of original Brillouin zone. The zone folding is shown in the inset figures in Fig. 2.10. Using monolayer BP as an example, we show how bands are folded from Γ point to Y point.
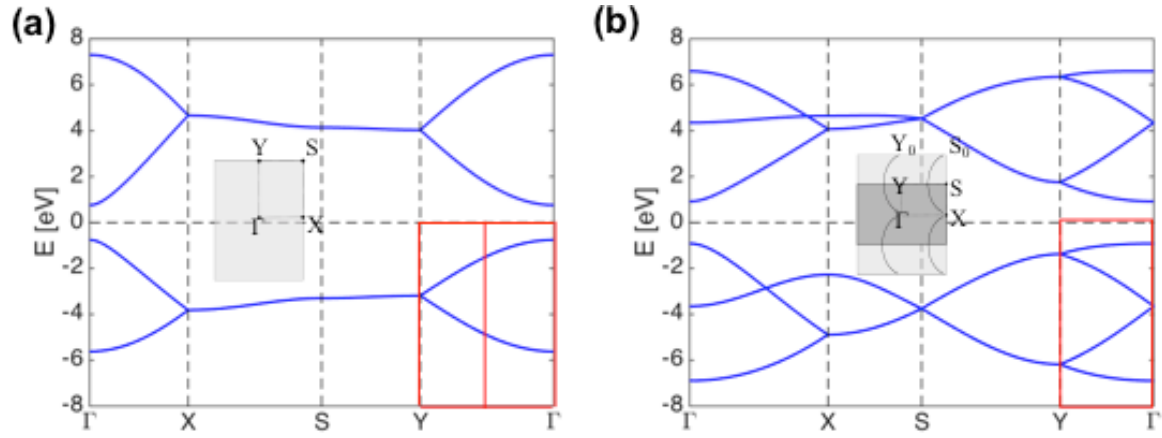
Figure 2.10 (a) Monolayer band structure using simplified tight-binding parameters. (b) Monolayer band structure using advanced tight-binding parameters. The red panels show how bands are folded from Γ to Y point. The inset figures show the _k_ space folding.

Chapter 3 Performance Limit of Few-Layer Phosphorene FETs

3.1 Motivation

Recent experiments of few-layer phosphorene FETs exhibited promising device characteristics such as large current ratio (maximum $I_{on}/I_{off} \sim 10^5$) and high field-effect mobility (up to 1,000 cm^2/V-s at room temperature) [14], [15]. On the other hand, performance limits of phosphorene FETs have been projected through numerical device simulations [26]–[28]. However, most theoretical studies have focused on monolayer phosphorene FETs, and little is known about few-layer phosphorene devices [29]. In particular, the role of multiple layers in the device performance is vague due to the trade-off of the channel thickness: Multiple layers may deliver a higher current than a monolayer because of larger density of states, but at the same time, the thicker channel has a disadvantage in electrostatic control by the gate. Moreover, atomistic quantum transport simulation of few-layer phosphorene FETs is currently absent, and the scaling limit of such devices is unknown. This calls for careful investigation of few-layer phosphorene FETs using rigorous atomistic quantum transport simulations to develop advanced knowledge of novel phosphorene devices towards proper design optimization and performance engineering.

In this chapter, we investigate the transport characteristics of bilayer phosphorene FETs, which are essentially different from monolayer devices, representing the simplest form of few-layer FETs. We use two different device structures of single-gate (SG) and double-gate (DG) device geometries and compare their device performance. Various equivalent oxide thickness (EOT) and channel length (L$_{ch}$) are used to investigate the scaling limit of bilayer phosphorene FETs, and our simulation results reveal that bilayer phosphorene FETs can be scaled down to ~8 nm without significant degradation in the off-state characteristics. We also benchmark bilayer phosphorene FETs against monolayer phosphorene and bilayer transition metal dichalcogenide (TMDC) FETs, which reveals that the bilayer phosphorene FET outperforms other similar 2D devices based on bilayer TMDC semiconductors, making both monolayer and bilayer phosphorene FETs strong contenders for next-generation switching devices.

3.2 Simulation Settings

Transport properties of FETs are simulated based on the non-equilibrium Green's function (NEGF) formalism with a tight-binding approximation, self-consistently with Poisson's equation. We use five intralayer hopping parameters ($t_1 = -1.220$ eV, $t_2 = 3.665$ eV, $t_3 = -0.205$ eV, $t_4 = -0.105$ eV, $t_5 =$

−0.055 eV) for each layer, and four additional parameters ($t_{\perp 1} = 0.295$ eV, $t_{\perp 2} = 0.273$ eV, $t_{\perp 3} = -0.151$ eV, $t_{\perp 4} = -0.091$ eV) to describe the interlayer coupling of bilayer phosphorene ($E_g = 1.12$ eV) [25]. Charge density and current are calculated by the numerical summation of transverse momentum [30], for which equally spaced 800 points are taken within the first Brillouin zone. Open boundary condition is treated by contact self-energies, which are numerically calculated using the Sancho-Rubio method [31]. The potential of each layer in bilayer phosphorene is independently treated in atomistic resolution in Poisson's equation, which is in turn combined with the Green's function for the transport calculation. Two different transport directions are considered: $\Gamma \rightarrow X$ (referred to as X direction in the subsequent discussion) and $\Gamma \rightarrow Y$ (similarly, Y direction). Figure 3.1 depicts the atomistic structure of bilayer phosphorene, where X and Y directions are specified. We use a SG structure with SiO$_2$ insulator ($\kappa \approx 3.9$), like most experiments [14]–[16], and a DG structure with high-k gate dielectric is also considered to examine how device performance can be improved beyond the recent experimental settings. Source and drain are 15-nm long and p-doped with $N_{S/D} = 2 \times 10^{20}$ cm^{-3} (most experiments exhibited p-type behaviors [14], [15]). Channel length is 10 nm for the nominal device and is varied from 4 to 20 nm for a scaling study. The gate oxide thickness is 3.14 nm for both SG and DG structures. Ballistic transport is assumed due to short channel lengths. Power supply voltage of $V_{DD} = 0.5$ V is used, and the room temperature is assumed.

(a)   **(b)**
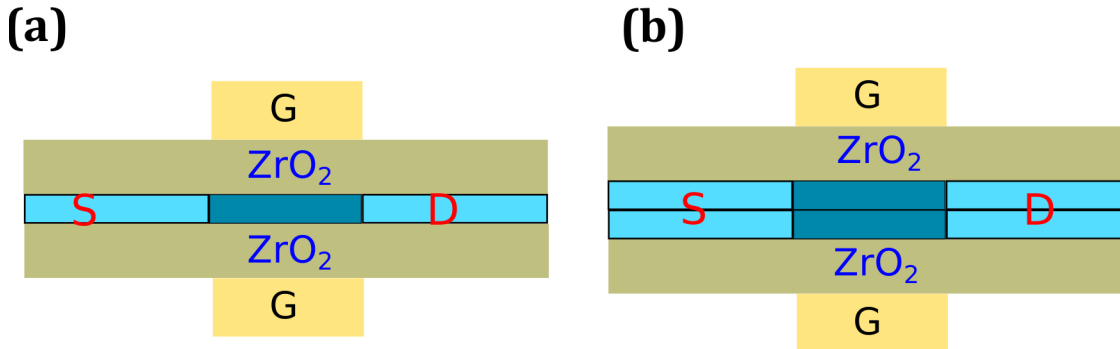
Figure 3.1 Device structure of (a) monolayer and (b) bilayer BP FET with double-gate geometry with 3-nm-thick ZrO$_2$ (κ=23) insulator. Source/drain and channel lengths are $L_{S/D}$ = 15 and L_{ch} = 10 nm, respectively. Source and drain are p-doped with $N_{S/D}$ = 2×10^{20} cm^{-3}. V_{DD} is −0.5 for PMOS [32].

3.3 Device Performance of Monolayer and Bilayer BP

Figure 3.2(a) shows the transfer characteristics of bilayer phosphorene FETs using a SG and a DG device structure in X transport direction. Although a SG bilayer phosphorene FET can exhibit reasonably good characteristics (*i.e.*, maximum achievable current ratio $> 10^6$, $I_{on} > 1$ mA/μm), our simulation shows that there exists significant room to improve the overall device performance through a better electrostatic control: By using a DG device structure with ZrO_2 dielectric ($\kappa = 23$), SS (= $\partial V_G / \partial \log_{10}(I_D)$) can be close to the ideal value (66 mV/dec rather than 124 mV/dec), I_{on} can be even larger (>3 mA/μm), and transconductance ($g_m = \partial I_D / \partial V_G$ at $I_D = 1$ mA/μm) can be increased from 3.4 to 14.7 mS/μm. Due to the anisotropic nature of bilayer phosphorene band structure [18], we also examined the transport properties in Y direction in Fig. 3.2(b), where we can observe the same trend as in X direction. Figure 3.2(c) shows I_{on} vs. I_{on}/I_{off} for all four devices considered in Figs. 3.2(a) and 3.2(b). It clearly demonstrates that DG structures (dashed lines) can provide significantly larger I_{on}/I_{off} at the same on current (*e.g.*, I_{on}/I_{off} increases by 10^5 at $I_{on} = 1$ mA/μm). We can also point out that, for the proper operation range (*i.e.*, $I_{on} >$ a few hundreds of μA/μm), X direction is preferable in terms of large I_{on} and I_{on}/I_{off}, which is attributed to smaller effective mass of bilayer phosphorene in X direction than in Y direction [18]. The multi-gate structure can improve not only the transfer characteristics but also output characteristics. Figure 3.2(d) shows a clear saturation behavior using the DG geometry with 77% smaller output conductance, g_d (= $\partial I_D / \partial V_D$), as compared to the SG device.
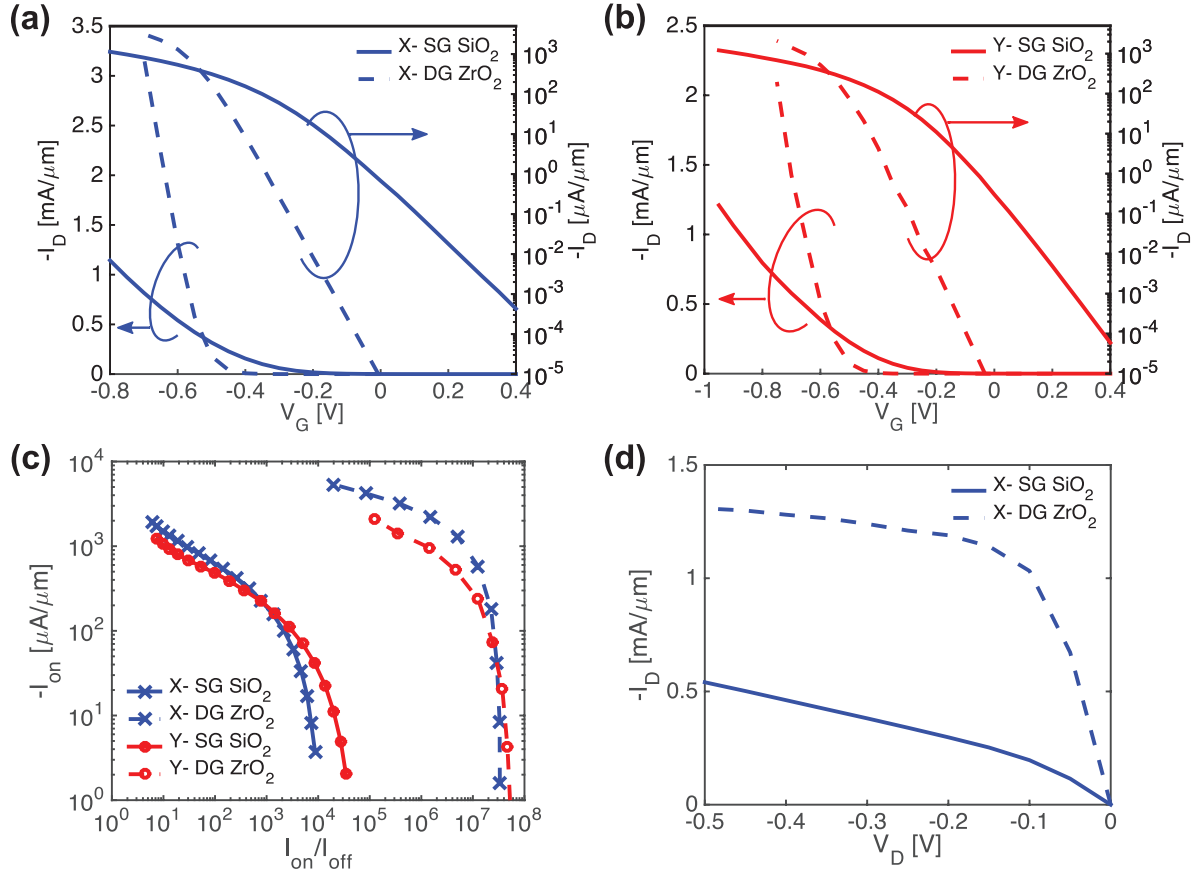
Figure 3.2 Device characteristics of bilayer phosphorene FETs. $I_D - V_G$ **plots for SG (solid line) and DG (dashed line) bilayer phosphorene FETs in (a) X and (b) Y direction at** V_D = -0.5 V. (c) I_{on} **vs.** I_{on}/I_{off} **for the four devices shown in (a) and (b). (d)** $I_D - V_D$ **curves of bilayer phosphorene FETs in X direction for SG (solid) and DG (dashed) structures at** V_G = -0.6 V [33].

3.4 Effect of L_{ch} and EOT Variation

Next, we perform a scaling study of bilayer phosphorene FETs. EOT is one of the key parameters determining the overall device performance, and therefore, we first investigate the scaling of EOT using three different materials: ZrO_2, Al_2O_3 (κ = 9), and SiO_2 without changing the thickness (3.14 nm). Figure 3.3(a) shows g_m and SS as a function of EOT, where our detailed simulations reveal that, as EOT scales down from 3.14 to 0.53 nm, g_m increases by 2.3 times and SS decreases from 91 to 66 mV/dec. Another key device parameter is channel length, and therefore, we also investigate the effects of channel length scaling by varying L_{ch} from 20 nm down to 4 nm, using ZrO_2 gate dielectric. Figure 3.3(b) shows the V_{th} roll-off as channel length decreases. The threshold voltage of bilayer

phosphorene FET is -0.57 V at L_{ch} > 15 nm, and it monotonically increases as L_{ch} decreases, eventually becoming -0.43 V at L_{ch} = 4 nm. Figure 3.3(c) shows SS and drain-induced barrier lowering, or DIBL = $\Delta V / \Delta V_D$ (at I_{off} = 0.1 nA/μm), as a function of channel length. For the device with L_{ch} > 15 nm, SS is close to the theoretical limit of 60 mV/dec. It gradually increases as channel length scales down to ~8 nm, but it shows a sudden rise at ~6 nm, resulting in SS > 100 mV/dec at L_{ch} < 6 nm. The same trend can also be observed for DIBL. Therefore, we can conclude that bilayer phosphorene FETs can be scaled down only to ~8 nm for better performance without significant short-channel effects. Figure 3.3(d), which is energy-resolved current spectrum, $I(E)$ (bottom axis) with valence band (E_v) profile along the device (top axis) for 6-nm channel, clearly explains the reason. At L_{ch} < 8 nm, there exists a significant direct tunneling current from the source to the drain, and therefore, bilayer phosphorene FETs exhibit the V_{th} roll-off and the significant increases of SS and DIBL.
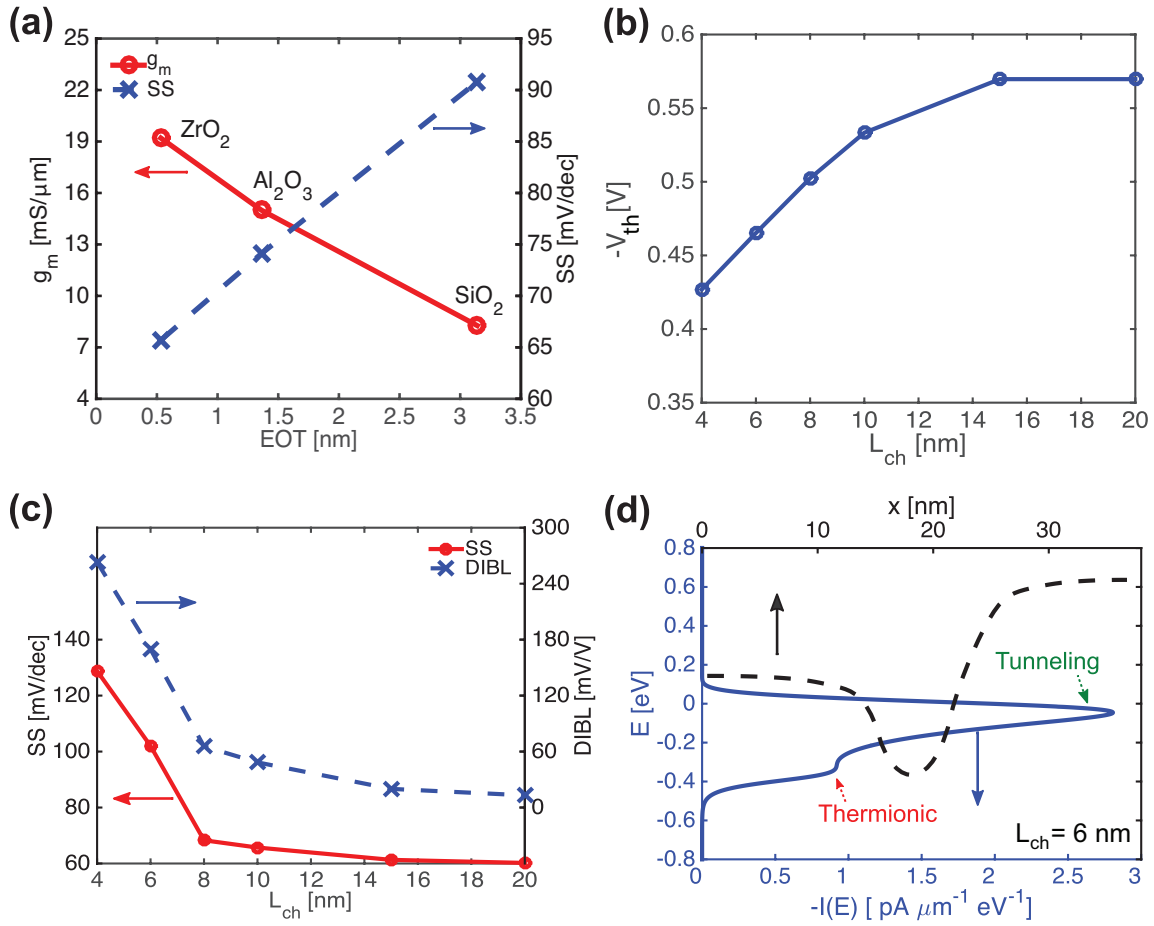
Figure 3.3 Scaling of bilayer phosphorene FETs (using DG structure in X direction). (a) Transconductance g_m (solid line with circles; left axis) and subthreshold swing SS (dashes line with crosses; right axis) as a function of EOT. (b) Threshold voltage V_{th} at various channel lengths. (c) SS (solid line with circles; left axis) and DIBL (dashed line with crosses; right axis) vs. L_{ch}. In (b) and (c), ZrO_2 is used for gate dielectric. (d) Energy-resolved current spectrum (solid line; bottom axis) and valence band (E_v) profile along the device (dashed line; top axis) for 6-nm channel at $V_G = 0$ V [33].

3.5 Comparison with TMDC FETs

It will be instructive to benchmark bilayer phosphorene FETs against other similar 2D semiconductor FETs. First, we compare monolayer and bilayer phosphorene FETs in Fig. 4(a), where both devices exhibit nearly ideal switching characteristics with SS = 62–66 mV/dec as well as excellent on-state characteristics (I_{on} being a few mA/µm; $g_m > 12$ mS/µm). For a comprehensive

32

analysis, we have plotted I_{on} vs. I_{on}/I_{off} in Fig. 3.4(b), which shows that both devices are equally attractive for switching applications under the proper electrostatic control. However, we expect that few-layer phosphorene FETs with a larger EOT can exhibit smaller I_{on} than the monolayer device at the same I_{on}/I_{off}, as shown for TMDC FETs [34]. Such penalty with multi-layers can result from the degradation of off-state characteristics rather than the on-state performance [26] due to nearly identical effective mass for few-layer phosphorene [18]. In light of this, we compared SS of few-layer phosphorene FETs (Table 3.1) using effective mass approximation. Although SS increases significantly with the number of layers with SiO_2 gate dielectric, it remains nearly ideal (64-69 mV/dec) with an excellent electrostatic control through ZrO_2 gate oxide, indicating the potential of few-layer phosphorene FETs for switching applications.
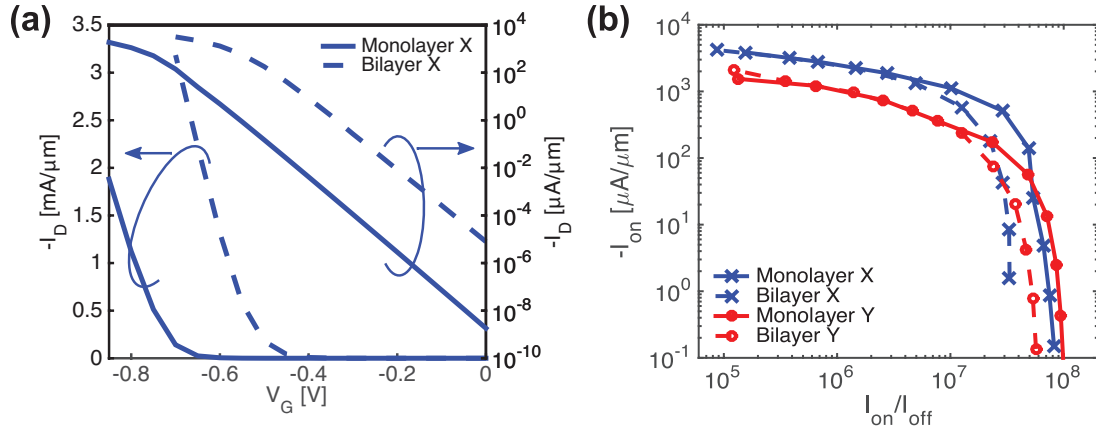
Figure 3.4 Performance comparison of monolayer and bilayer phosphorene DG FETs. (a) $I_D -$ V_G plots for monolayer (solid line) and bilayer (dashed) phosphorene FETs in X direction at V_D = -0.5 V. (b) I_{on} vs. I_{on}/I_{off} of monolayer and bilayer phosphorene FETs in X and Y transport directions [33]**.**

Finally, we benchmark bilayer phosphorene FETs against other devices based on bilayer TMDC semiconductors, *i.e.*, MoS_2 and WSe_2 [34], using the same device parameters (L_{ch} = 9 nm, EOT = 0.5 nm with a SG device structure, V_{DD} = 0.5 V). Table 3.2 shows that the bilayer phosphorene FET can deliver 13-20% larger I_{on} and I_{on}/I_{off} compared to bilayer MoS_2 and WSe_2 FETs, showing better switching characteristics. It is attributed mainly to the fact that effective mass of bilayer phosphorene is smaller than that of bilayer MoS_2 and WSe_2 [34]. We also added the last column in the Table 3.2 for the 8-nm-channel DG bilayer phosphorene FET as a reference.

Table 3.1 Subthreshold swing of few-layer phosphorene FETs [33]

Number of Layer		1	2	3	4
SS (mV/dec)	DG ZrO_2	64	66	67	69
	DG SiO_2	77	85	93	99

Table 3.2 Comparison of device parameters of bilayer TMDC and phosphorene FETs [33]

Channel Material	Bilayer MoS_2[†]	Bilayer WSe_2[†]	Bilayer phosphorene	Bilayer phosphorene
L_{ch} (nm)	9	9	9	8
EOT (nm)	0.5 (SG)	0.5 (SG)	0.5 (SG)	0.5 (DG)
I_{off} (μA/μm)	10^{-3}	10^{-3}	10^{-3}	10^{-3}
I_{on} (μA/μm)	210	198	238	988
I_{on}/I_{off}	2.1×10^5	2.0×10^5	2.4×10^5	9.9×10^5

[†]Gate length is 5 nm with 2-nm gate underlap on both sides [34].

3.6 Summary

We presented simulations of bilayer phosphorene FETs using self-consistent atomistic quantum transport simulations. Our results exhibited that 10-nm-channel bilayer phosphorene FETs can achieve excellent device characteristics such as $I_{on} >$ 3 mA/μm and SS ~66 mV/dec. While the scaling of gate dielectric monotonically improves the overall performance of the device, the channel length can be scaled down only to ~8 nm due to significant short-channel effects. Bilayer phosphorene FETs have favorable switching characteristics over other similar bilayer TMDC devices. It is expected that our comprehensive numerical study will provide the solid foundation for understanding phosphorene FETs, thereby creating useful insights into device design and experiments.

Chapter 4 Device Design Strategy towards High-performance and Low-power Applications

4.1 Motivation

Recently, 2D semiconductors such as molybdenum disulfide (MoS_2) or black phosphorus have been explored for future electronic device applications [16], [35]-[37] and they exhibited promising device characteristics such as high field-effect mobility ($\mu_{eff} > 1,000$ cm^2/V-s)[14], large on current ($I_{on} \sim 240$ µA/µm) [38], and large on-off current ratio ($I_{on}/I_{off} > 10^8$) [39]. However, most 2D-material electronic devices were studied individually without discussing the significance of the number of layers, and therefore, comprehensive design strategies for different target applications are currently absent, although the number of layers in 2D materials is strongly correlated to bandgap, density of states, and gate efficiency, which are key parameters determining the overall device performance. Thus, in this study, we will mainly discuss the engineering practice to optimize the number of layers in 2D-material electronic devices for different target applications.

Here we use layer of black phosphorus or phosphorene for active material of FETs. The device characteristics are investigated by means of self-consistent, atomistic quantum transport simulations using tight-binding approximation. In the last chapter, we used limited tight-binding parameters, which is tailored exclusively for mono- and bilayer phosphorene. In this chapter, we have carefully chosen tight-binding parameters that can rigorously describe the band structure of multilayer phosphorene as well as monolayer [19], in contrast to other previous studies where the electronic states were approximated with effective mass [40], $k \cdot p$ [29], [41], or limited tight-binding parameters [25], [27], [33], [42].

4.2 Simulation Method

Electronic states of few-layer phosphorene are described with a tight-binding approximation using ten intralayer hopping parameters ($t_1^{\parallel} = -1.486$ eV, $t_2^{\parallel} = 3.729$ eV, $t_3^{\parallel} = -0.252$ eV, $t_4^{\parallel} = -0.071$ eV, $t_5^{\parallel} = -0.019$ eV, $t_6^{\parallel} = 0.186$ eV, $t_7^{\parallel} = -0.063$ eV, $t_8^{\parallel} = 0.101$ eV, $t_9^{\parallel} = -0.042$ eV, $t_{10}^{\parallel} = 0.073$ eV) and four additional parameters ($t_1^{\perp} = 0.524$ eV, $t_2^{\perp} = 0.180$ eV, $t_3^{\perp} = -0.123$ eV, $t_4^{\perp} = -0.168$ eV) for interlayer coupling, which can provide accurate band structure for multilayers as well as mono- and bilayer phosphorene [19]. We have used the recursive Green's function algorithm [30], where tri-diagonal block matrix is required to find the numerical solution of the NEGF simulation efficiently. For this,

we have constructed a supercell, including two unit cells in y direction, to take into account the long-range interactions through $t_8^{\parallel}$ as shown in Fig. 4.1(a), which cannot be included if only the nearest unit cells are considered. By taking the supercell, the first Brillouin zone is reduced as shown in Fig. 4.1(b) due to zone folding, where Γ point is overlapped with the Y point of the unit cell (denoted as Y_0) and X point with the S point of the unit cell (S_0). The consequent band structures of mono-, bi-, and tetralayer phosphorene are shown in Figs. 4.1(c)–4.1(e) and the density of states (DOS) of the same materials are numerically calculated in Fig. 4.1(f). In this study, we have explored mono- to pentalayer phosphorene for the transistor applications, and their bandgaps and effective masses are shown in Table 4.1.
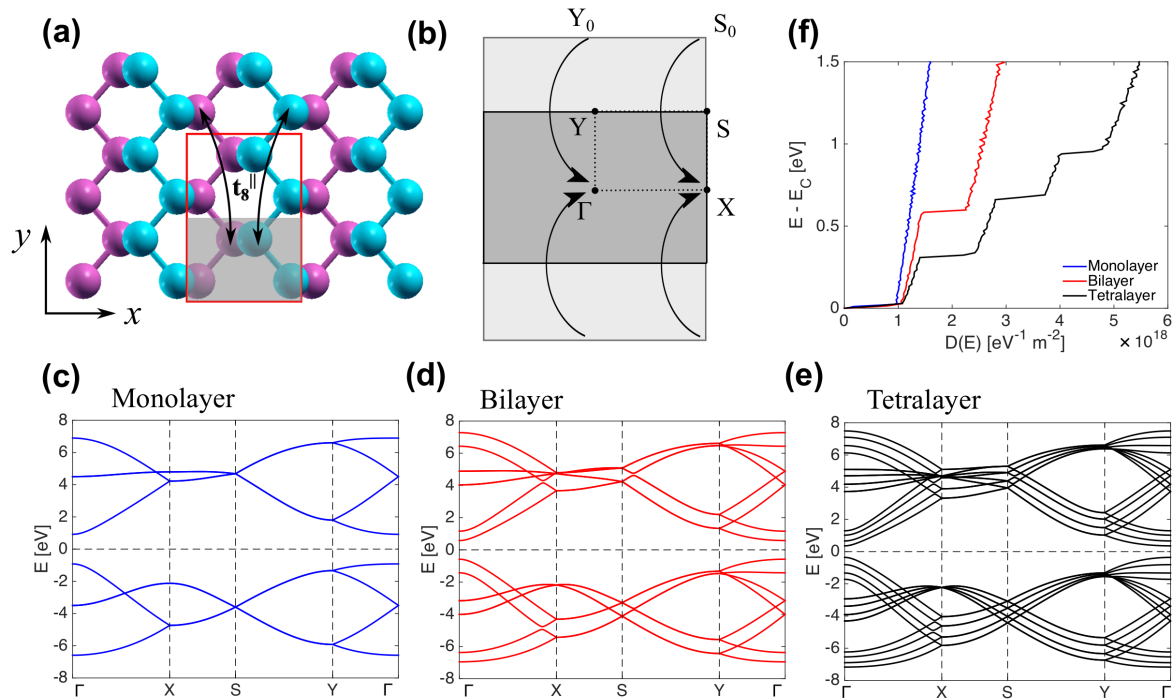
Figure 4.1 (a) Atomistic configuration of phosphorene (top view). Different colors are used for top (cyan) and bottom (dark pink) layer for visualization. The red rectangle shows the supercell that we have used in our simulation, which consists of two unit cells of phosphorene. A unit cell is shown by the shaded region. (b) The first Brillouin zone of phosphorene using the supercell (dark region) and the original unit cell (bright region), where arrows show zone folding. Band structure of (d) monolayer (e) bilayer and (f) tetralayer phosphorene plotted using the supercell. (f) Density of states (DOS) of monolayer, bilayer and tetralayer phosphorene near the conduction band edge [43]**.**

Table 4.1 Bandgap and effective mass of mono- to pentalayer phosphorene in Γ→X transport direction [43]

Number of Layers	1	2	3	4	5
E_g (eV)	1.84	1.16	0.87	0.72	0.63
m_e^* $(m_0)^\dagger$	0.19	0.18	0.17	0.16	0.15
m_h^* $(m_0)^\dagger$	0.2	0.17	0.16	0.15	0.14

†*m_0 is free electron mass.*

Transport characteristics of mono- to pentalayer phosphorene FETs are simulated based on non-equilibrium Green's function (NEGF) formalism [24], where the Hamiltonian matrix is constructed using the supercell as described above. The ballistic transport equation is solved iteratively with Poisson's equation until self-consistency between the charge and the electrostatic potential is satisfied. We considered Γ→X to be the direction of transport, which is also referred to as the armchair direction in literature [26], [27]. Charge density and current are calculated by the numerical summation of transverse modes. Two different device structures are considered: conventional FET structure for high-performance applications and tunnel FET structure for low-power applications. The nominal device has 15-nm channel length (L_{ch}) and 20-nm source/drain extensions. The source and drain are *n*-doped in conventional FETs, and *p*-doped source and *n*-doped drain are used for the TFETs. The doping concentration at source and drain ($N_{S/D}$) is 1.6×10^{13} cm^{-2}. We use a single gate (SG) for conventional FETs (Fig. 4.2(a)) following the recent experimental demonstrations [14], [44], whereas a double-gate (DG) device geometry (Fig. 4.2(b)) is assumed for TFETs because the electrostatic control is critical for abrupt switching in low-power devices [45], [46]. In both devices, 3.14-nm ZrO$_2$ ($\kappa \approx 23$) or an equivalent oxide thickness (EOT) of ~0.5 nm is used and the dielectric constant of phosphorene is 10 [47]. Scattering is ignored since it is expected that our devices will be operated in ballistic or quasi-ballistic regime due to short channel lengths considered in this study. For long-channel devices, scattering mechanism can reduce the drain current and also limit the minimum leakage current and subthreshold swing, but its impact will be minimal for the size of devices considered here. It is assumed that devices are operated at room temperature (300 K).
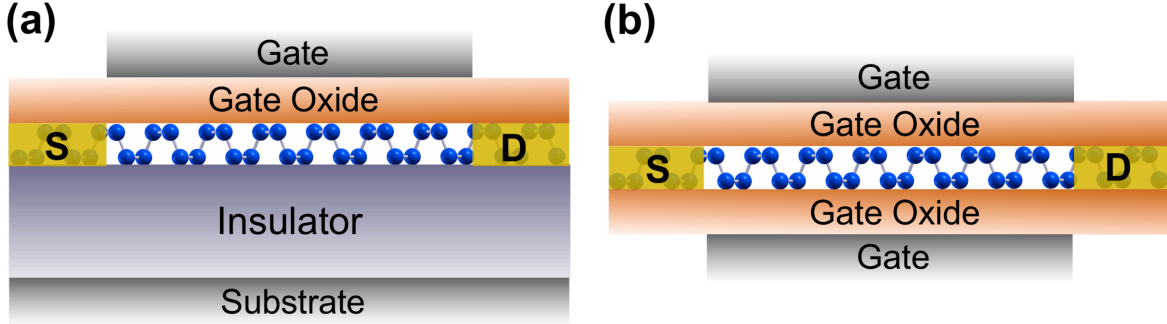
Figure 4.2 Device structure of phosphorene field-effect transistors (FETs) with (a) single-gate (SG) and (b) double-gate (DG) geometry. We have used mono- to pentalayer phosphorene for the channel material (monolayer is shown here) [43]**.**

4.3 High-performance Applications

We focus on high-performance applications using a conventional FET structure based on phosphorene, where we investigate the impact of channel thickness on various device performance such as on current, subthreshold behavior, and minimum leakage current. In general, for fast switching speed, large density-of-states (DOS) materials are favorable for the channel and multiple layers could satisfy such a requirement. However, at the same time, thicker channel can result in a poor gate electrostatic control, increasing the leakage current significantly. Therefore, both on and off states should be simultaneously investigated in designing high-performance 2D-material FETs to maximize the device performance.

4.3.1 On-state Device Performance

First, we investigated the device characteristics of conventional FETs using various numbers of phosphorene layers for the channel material. Figures 4.3 (a) and (b) are transfer characteristics of mono-, bi- and tetralayer conventional FETs in linear and log scale, respectively. In terms of on-state characteristics, no remarkable difference is observed among the devices where $I_{on} > 1$ mA/μm and g_m ~15 mS/μm. This is because few-layer phosphorenes have almost identical electron effective masses (Table 4.1) and DOS near the conduction band edge (at $E - E_c < 0.3$ eV in Fig. 4.1(f)) where the majority of carrier flows. Although multilayer phosphorene has larger DOS than monolayer phosphorene at higher energy levels, its impact on the I_{on} is minimal since the relevant energy states are too far from the conduction band minima.
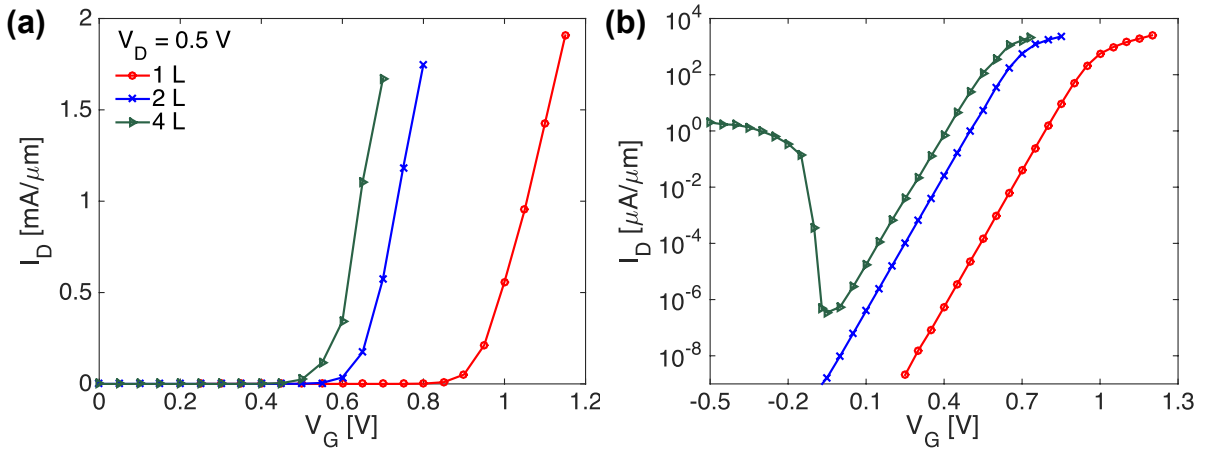
Figure 4.3 I_D–V_G **plots of conventional FETs based on monolayer (1L; line with circles), bilayer (2L; line with crosses) and tetralayer phosphorene (4L; line with triangles) shown in (a) linear and (b) logarithmic scale** [43].

4.3.2 Leakage Current at Off-state

On the other hand, we can observe dissimilar off-state characteristics with different numbers of phosphorene layers. In particular, the minimum leakage current can be significantly increased if thicker phosphorene is used due to the smaller bandgap. Figure 4.3(b) shows that, as the gate voltage is lowered, the off current of tetralayer phosphorene FET monotonically decreases to ~10^{-6} μA/μm, but I_{off} increases significantly beyond this point if the gate voltage is decreased further at $V_G < -0.05$ V. This is gate-induced drain leakage (GIDL) that is caused by band-to-band tunneling in small-bandgap materials [41], [48]. We have plotted conduction and valence bands on top of the local density of states (LDOS) of the tetralayer phosphorene FET at $V_G = -0.5$ V in the left panel of Fig. 4.4(a), and the corresponding energy-resolved current spectrum is shown on the right. It is clearly shown that the tunneling current is significantly larger than thermionic current (which cannot be even observed in the current spectrum due to its negligible contribution to the total current). In comparison, FETs based on larger-bandgap materials like mono- or bilayer phosphorene have more immunity to GIDL and the minimum leakage current can be significantly smaller than that of multilayer phosphorene FETs.
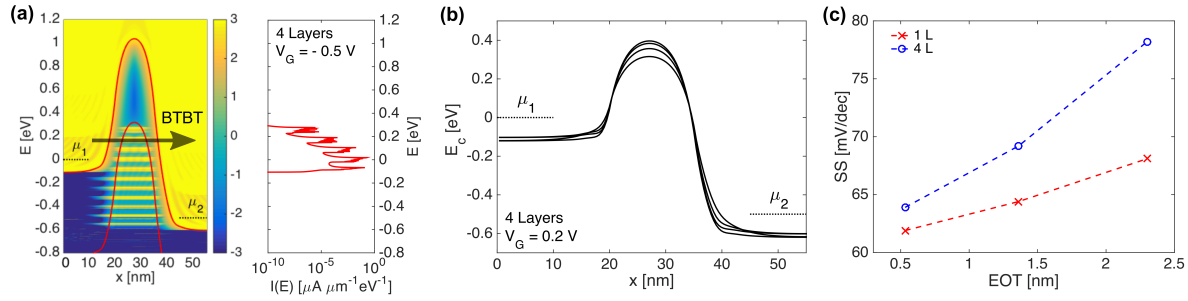
Figure 4.4 (a) (Left) Conduction (E_c) and valence band (E_v) of tetralayer phosphorene FET plotted on local density of states (LDOS; in log scale) at $V_G = -0.5$ V and $V_D = 0.5$ V, where E_c and E_v are the average potential of four layers. $\mu_{1,2}$ are chemical potentials at source and drain, respectively. The arrow indicates band-to-band tunneling (BTBT). (Right) The corresponding energy-resolved current spectrum. (b) Conduction band profile of each layer (without taking the average) along the device in the tetralayer phosphorene FET at $V_G = 0.2$ V and $V_D = 0.5$ V. (c) Subthreshold swing (SS) of monolayer and tetralayer phosphorene FETs at various equivalent oxide thickness (EOT) [43].

4.3.3 Off-state Device Performance

Subthreshold swing (SS) is one of the most important device characteristics at off state. Thicker phosphorene shows larger subthreshold swing, although the difference is insignificant with EOT of 0.5 nm: SS = 61.9, 62.3, and 63.9 mV/dec for mono-, bi-, and tetralayer phosphorene, respectively. This lower efficiency of the electrostatic control by the gate in tetralayer phosphorene FETs can be observed in Fig. 4.4(b), which clearly depicts that the electrostatic potential of each layer is controlled non-uniformly by the gate, unlike the monolayer FET. Even with very thin EOT, the potential barrier heights show ~0.1 eV difference between the top and the bottom layers. As the EOT becomes thicker, the performance degradation of gate electrostatic control in the tetralayer phosphorene becomes more conspicuous, which can be seen in Fig. 4.4(c), where SS of tetralayer phosphorene FET at 2.3-nm EOT is 22% larger than that at EOT = 0.5 nm, while monolayer shows only 10% increase for the same change.

4.3.4 Summary on High-performance Devices Design Strategies

In view of the above results, we can conclude that monolayer can provide the best device characteristics in phosphorene-based conventional FETs toward high-performance applications due to

the following reasons: (i) Monolayer guarantees the best electrostatic control by the gate, resulting in the abrupt switching characteristics near the classical limit. (ii) Multilayer phosphorene suffers from GIDL or band-to-band tunneling due to its small bandgap, which is not observed in the monolayer phosphorene FET. (iii) In addition, monolayer phosphorene does not show any drawback in on current and transconductance despite its relatively lower DOS, as compared to multilayer phosphorene. From this perspective, engineering the number of layers in phosphorene-based conventional FETs can be straightforward. However, things are getting more complicated if tunnel FETs are taken into account, which will be discussed next in detail.

4.4 Low-power Applications

Engineering tunnel FETs (TFETs) by varying the number of layers could be more complicated because trade-off exists between the thickness and the bandgap of 2D materials [49]. In principle, monolayer can provide the best switching behavior, but its on current can be significantly limited by the large bandgap, rendering it impractical. On the other hand, multilayer phosphorene can suffer from large leakage current and poor electrostatic control, resulting in small on-off current ratio (I_{on}/I_{off}), which is not desirable for low-power switching devices. Therefore, we carry out comprehensive engineering practices to optimize the performance of phosphorene TFETs by varying material and device parameters such as number of layers, power supply voltage, doping concentration, and channel length.

4.4.1 Device Performance with Common V_{DD}

We first compare device performance of mono- to pentalayer phosphorene TFETs using a common power supply voltage (V_{DD}) of 0.4 V, which is the maximum drain voltage (V_D) that can be used for the pentalayer phosphorene (the smallest bandgap material considered in this study) TFET to avoid significant leakage at off state. This limitation is clearly shown in Fig. 4.5(a), which is the band profile of a pentalayer phosphorene TFET at the off state with the minimum leakage current, where significant leakage current would be inevitable if a larger V_D was applied. The transfer characteristics of mono- to pentalayer phosphorene TFETs are plotted in Fig. 4.5(b), where pentalayer shows the largest on current and also the largest leakage current due to the smallest bandgap. On the other hand, the large bandgap of monolayer phosphorene (1.84 eV) imposes a huge tunnel barrier even at high gate voltages, rendering it impractical for electronic devices under the give condition. Thus, we have plotted the subthreshold swing only for the rest four devices in Fig. 4.5(c), where bi- to pentalayer

41

phosphorene TFETs shows SS in the range of 30–43 mV/dec. Although thicker channel gradually loses electrostatic control, even the pentalayer device exhibited a reasonably good switching characteristic. In general, thinner phosphorene TFETs can provide larger maximum achievable I_{on}/I_{off}, but its on current can be significantly limited compared to thicker phosphorene devices as shown in Fig. 4.5(d), which indicates that I_{on} can be improved with more number of layers by sacrificing the on-off current ratio.
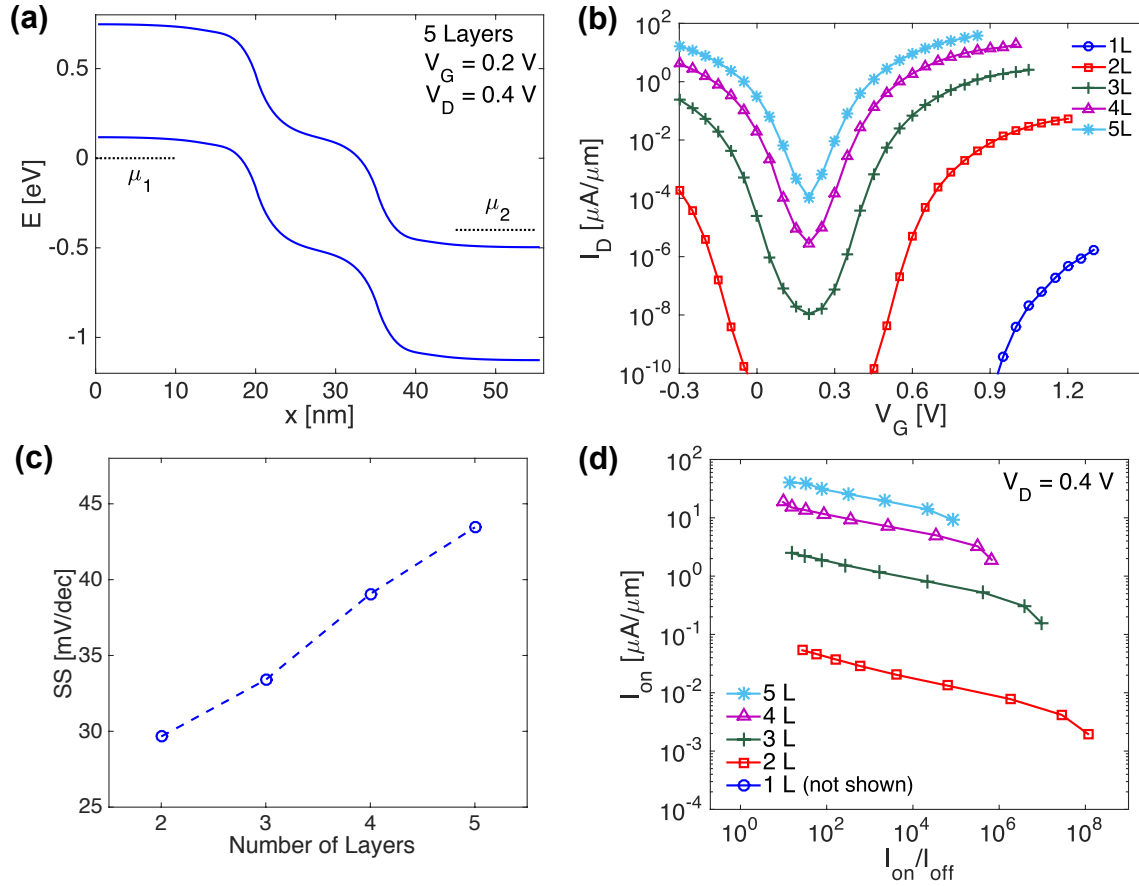
Figure 4.5 (a) The conduction and the valence band profile for pentalayer phosphorene TFET at $V_G = 0.2$ V and $V_D = 0.4$ V. (b) I_D–V_G characteristics for mono- to pentalayer phosphorene TFETs at $V_D = 0.4$ V. (c) The subthreshold swing of bi- to pentalayer phosphorene TFETs. (d) I_{on} vs. I_{on}/I_{off} of phosphorene TFETs at $V_D = 0.4$ V. Monolayer is out of range in this plot due to its extremely small I_{on} [43].

4.4.2 Device Performance with Different V_{DD}

In the above discussion, for a comparison of phosphorene TFETs with different number of layers, we used a common V_D, which limited the achievable range in I_{on}/I_{off}, particularly for large bandgap materials. In principle, for the same on current, larger I_{on}/I_{off} can be achieved by using a larger V_D, since the device can be operated within a larger voltage window. Figure 4.6(a) is I_D–V_G characteristics of the trilayer phosphorene TFET at two different drain voltages of 0.4 V (solid line) and 0.6 V (dashed line), which clearly shows that I_{on}/I_{off} can be significantly increased with $V_D = 0.6$ V for the common I_{on} of 1.6 µA/µm (at $V_{on} = 0.9$ V). Moreover, a larger I_{on} can also be achieved at $V_D = 0.6$ V, as compared with $V_D = 0.4$ V, due to the larger energy window for current flow at higher gate voltages as shown in Fig. 4.6(b). Therefore, to take the advantages of large V_D, we have used different drain voltages for different numbers of phosphorene layers: $V_D = 0.7$ V for mono- and bilayer, 0.6 V for trilayer, 0.5 V for tetralayer, and 0.4 V for pentalayer phosphorene TFETs. The corresponding I_{on} vs. I_{on}/I_{off} is shown in Fig. 4.6(c). We have observed that, for bilayer phosphorene TFET, the maximum achievable I_{on}/I_{off} is significantly increased by more than one order of magnitude and I_{on} is also increased by a factor of 40 for the same $I_{on}/I_{off} = 10^8$ using a larger V_D. However, such a dramatic improvement of maximum achievable I_{on}/I_{off} was not observed in tri- and tetralayer phosphorene TFETs with the increased drain voltages. This is due to the larger minimum leakage current (I_{min}) at larger V_D, as can be seen in Fig. 4.6(a), which is attributed to the larger energy window for the direct tunneling from source to drain. In Fig. 4.6(c), we classified phosphorene TFETs into two groups: Three or more numbers of phosphorene layers TFETs (Group A) show reasonably high on current but relatively low I_{on}/I_{off}; bilayer phosphorene TFET is another group (Group B) that can provide a large I_{on}/I_{off} but a limited I_{on}. In the subsequent discussion, we will employ different strategies for these two groups to enhance the device performance of phosphorene TFETs.
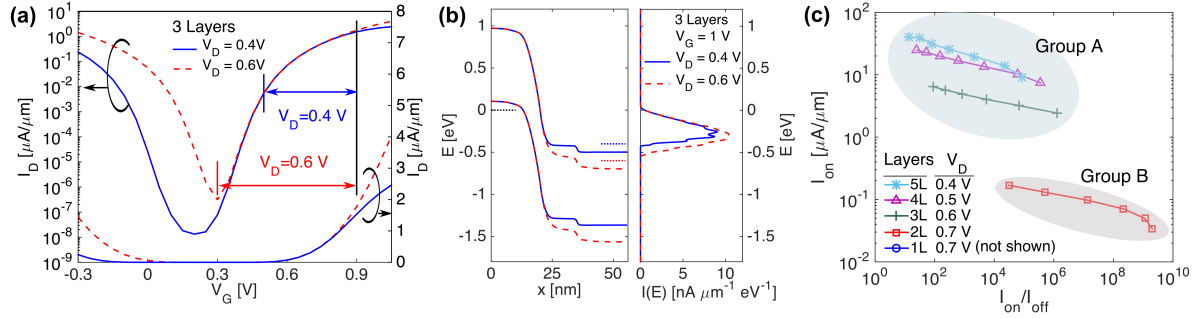
Figure 4.6 (a) I_D–V_G **characteristics of trilayer phosphorene TFETs at** $V_D = 0.4$ **V (solid line) and** $V_D = 0.6$ **V (dashed line), shown in logarithmic scale (left axis) and linear scale (right axis). (b) Energy-resolved current spectrum (right panel) shown with the** E_c **and** E_v **profiles along the device (left panel) for the trilayer phosphorene TFET for** $V_D = 0.4$ **V (solid line) and 0.6 V (dashed line) at** $V_G = 1$ **V. (c)** I_{on} **vs.** I_{on}/I_{off} **of phosphorene TFETs with various drain voltages carefully chosen for different numbers of layers:** $V_D = 0.7$ **V for mono- and bi-layer, 0.6 V for trilayer, 0.5 V for tetralayer, and 0.4 V for pentalayer, respectively. Monolayer is out of range in this plot due to the extremely small** I_{on} [43]**.**

4.4.3 Optimization for Group A

In principle, the leakage current of a ballistic TFET can be suppressed by increasing channel length without degrading the on-state characteristics, and therefore, we have varied L_{ch} from 15 to 25 nm for tri- to pentalayer phosphorene TFETs (Group A) using the same drain voltages as given in Fig. 4.6(c). The I_D–V_G characteristics are shown for trilayer phosphorene TFETs with different channel lengths in Fig. 4.7(a), where the minimum leakage current decreases exponentially as L_{ch} increases. We have repeated the same also for tetra- and pentalayer phosphorene TFETs and plotted I_{on} vs. I_{on}/I_{off} in Fig. 4.7(b). It is shown that, while I_{on} remains intact, the maximum achievable I_{on}/I_{off} is significantly increased for all three devices with 25-nm channel, up to 4 orders of magnitude for the trilayer phosphorene. In addition, subthreshold swing is also decreased significantly from 35 to 15 mV/dec by increasing the channel length from 15 to 25 nm for trilayer phosphorene TFETs (Fig. 4.7(c)).

44
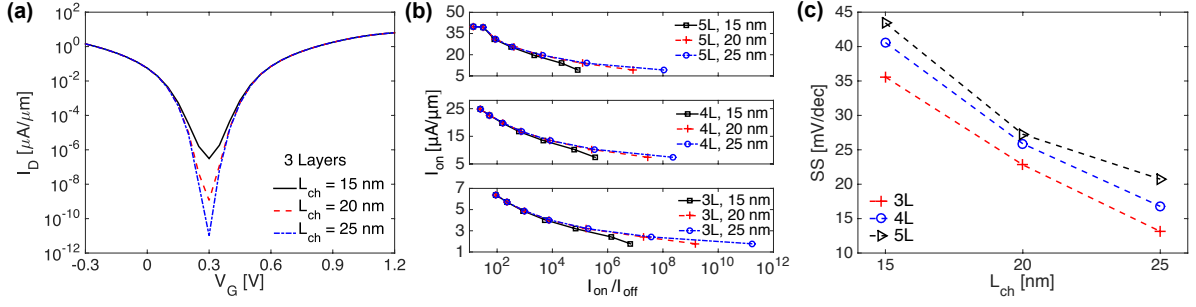
Figure 4.7 (a) I_D–V_G **characteristics of trilayer phosphorene TFETs for** L_{ch} **= 15 nm (solid line), 20 nm (dashed line) and 25 nm (dash-dot line) at** V_D **= 0.6 V. (b)** I_{on} **vs.** I_{on}/I_{off} **for trilayer (lower panel), tetralayer (middle panel) and pentalayer (upper panel) phosphorene TFETs with** L_{ch} **= 15–25 nm at** V_D **shown in Fig. 4.6(c). (c) Subthreshold swing as a function of channel length for the devices shown in (b)** [43]**.**

4.4.4 Optimization for Group B

One of the common issues in TFETs is relatively small on current due to the large tunnel barrier even at large gate voltages, which is exactly what we have observed particularly with the bilayer phosphorene TFET (Group B). In order to overcome such a limitation, barrier-free tunneling based on carbon heterostructure has been proposed earlier [50]. However, the same approach cannot be applicable to phosphorene TFETs, and therefore, here the similar effects will be achieved by increasing doping concentration at source and drain to enhance the I_{on} of bilayer phosphorene TFETs. A 15-nm channel and the same drain voltage is used as in Fig. 4.6(c). Figure 4.8(a) shows the significant upward shift of I_D–V_G curve for bilayer phosphorene TFETs (dashed line and solid line with squares are for $N_{S/D}$ of 1.6×10^{13} cm^{-2} and 3.2×10^{13} cm^{-2}, respectively). Figure 4.8(b) shows that the increase of $N_{S/D}$ enormously enhanced the I_{on} of bilayer phosphorene TFET by two orders of magnitude with the cost of I_{on}/I_{off} by one order of magnitude. Figure 4.8(c) shows the enhancement of current spectrum at the on state (V_G = 1 V), the origin of which is barrier thinning at the source-channel junction as shown in Fig. 4.8(d), whereas the larger leakage current is attributed to the larger energy window for carrier injection opened by the larger $N_{S/D}$.
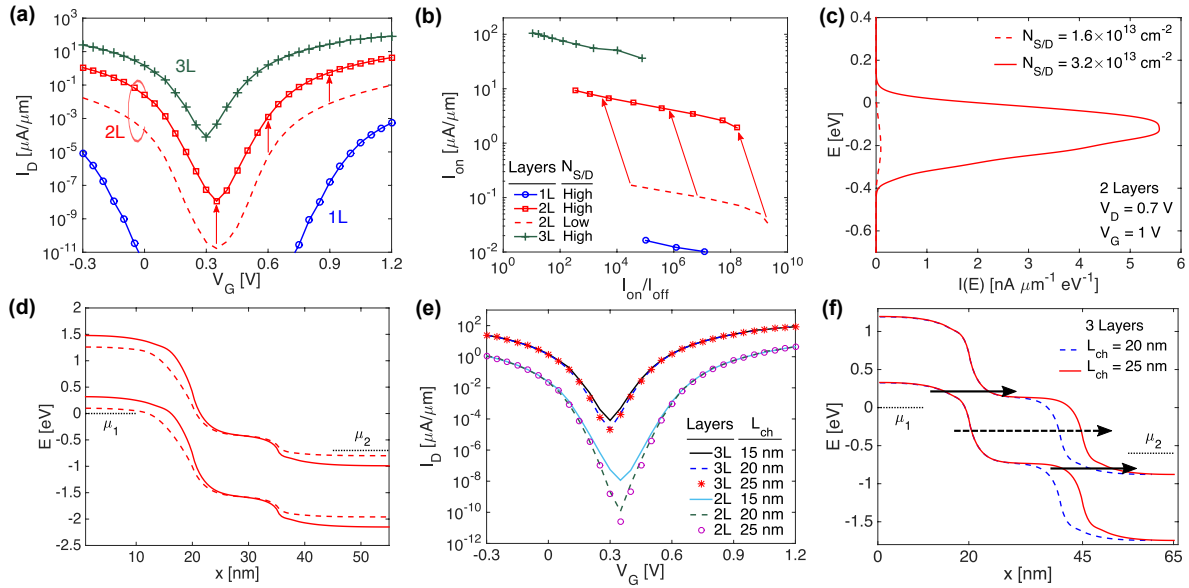
Figure 4.8 (a) I_D–V_G **characteristics for monolayer (solid line with circles), bilayer (solid line with squares) and trilayer (solid line with crosses) phosphorene TFETs with** $N_{S/D} = 3.2 \times 10^{13} \text{cm}^{-2}$. **Bilayer phosphorene TFET with** $N_{S/D} = 1.6 \times 10^{13} \text{cm}^{-2}$ **(dashed line) is also shown for a reference.** L_{ch} **is 15 nm and** V_D **is as shown in Fig. 4.6(c). (b)** I_{on} **vs.** I_{on}/I_{off} **for the devices shown in (a). (c) Energy-resolved current spectrum of bilayer phosphorene TFETs for different** $N_{S/D}$. **(d) Potential profile for the device shown in (c). (e)** I_D–V_G **characteristics of bi- and trilayer phosphorene TFETs for the channel lengths of 15, 20, and 25 nm with** $N_{S/D} = 3.2 \times 10^{13} \text{cm}^{-2}$. **(f) Potential profile along the device for trilayer phosphorene TFETs at the off state for the channel lengths of 20 nm (dashed line) and 25 nm (solid line). Dashed arrow illustrates direct leakage through the entire channel, and solid arrows indicate the additional leakage paths through the junction between the source/drain and the channel** [43].

It would be worth investigating mono- and trilayer phosphorene TFETs based on high $N_{S/D}$ in addition to the bilayer phosphorene TFET. Both devices exhibited significant improvement in on-state characteristics as shown in Figs. 4.8(a) and 4.8(b), but the I_{on} of monolayer phosphorene TFET still remained very low. We further engineered bi- and trilayer phosphorene TFETs with longer channel lengths to suppress the minimum leakage current. For trilayer phosphorene TFET, the channel length engineering for smaller I_{min} becomes less efficient with an increased doping concentration (Fig. 4.8(e)), as compared to low $N_{S/D}$ case (Fig. 4.7(a)), and there is almost no gain in I_{min}, particularly for the channel longer than 20 nm. This is due to the presence of additional leakage

paths as shown by the solid arrows in Fig. 4.8(f), making the channel length engineering ineffective. For bilayer phosphorene TFETs, however, we can see larger gains in suppressing I_{min} in Fig. 4.8(e), due to the larger bandgap and hence less amount of tunneling through the addition leakage paths. With the increased doping density, the bilayer phosphorene TFET exhibits similar device performance as that of the trilayer phosphorene TFET based on low doping concentration with the maximum I_{on}/I_{off} of ~10^{11} at $L_{ch} = 25$ nm.

4.5 Comparison of Phosphorene-Based Conventional FETs and TFETs

Finally, we compare the device performance of phosphorene-based conventional FET and TFET. For a conventional FET, monolayer phosphorene is taken since it can provide the best device performance as we have shown earlier, and we choose bilayer and trilayer phosphorene for TFETs due to the same reason. Figure 4.9(a) shows I_{on} vs. I_{on}/I_{off} of those three devices that we simulated in the previous sections A and B. It turns out that the conventional FET can have significantly larger I_{on} than TFETs, making it more appropriate for high-performance applications where fast switching speed is critical. On the other hand, bilayer and trilayer phosphorene TFETs exhibited significantly larger I_{on}/I_{off} compared to the conventional FET, indicating that they can be suitable for low-power applications where speed is less important but power consumption is the main concern. In addition, the subthreshold swing of TFETs can be significantly smaller than the best conventional FET, especially for longer channel lengths, as shown in Fig. 4.9(b). At $L_{ch} = 25$ nm, bilayer and trilayer phosphorene TFETs exhibit 64% and 78% smaller SS than the conventional FETs. This comparison of the best devices from different configurations clearly identifies the target applications of each device and also provides useful insights into various parameters including the number of channel layers to maximize the performance of phosphorene FETs.
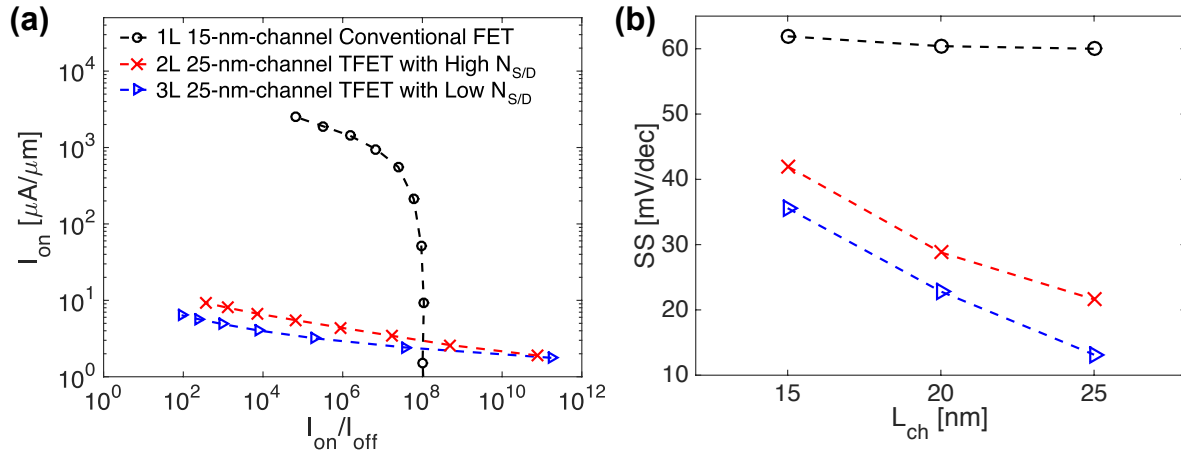
Figure 4.9 (a) I_{on} **vs.** I_{on}/I_{off} **for 15-nm-channel monolayer phosphorene conventional FET (dashed line with circles), 25-nm-channel bilayer phosphorene TFET with $N_{S/D} = 3.2 \times 10^{13} \text{cm}^{-2}$ (dashed line with crosses), and 25-nm-channel trilayer phosphorene TFET with $N_{S/D} = 1.6 \times 10^{13}$ cm^{-2} (dashed line with triangles). (b) Subthreshold swing of the devices shown in (a) at various channel lengths** [43]**.**

4.6 Summary

We explored mono- to pentalayer phosphorene FETs using self-consistent atomistic quantum transport simulations. We first examined the conventional FET structure and concluded that monolayer phosphorene can provide the best performance in every aspect. We showed that monolayer phosphorene FET can be switched near the classical limit of SS = 60 mV/dec with the large immunity to GIDL. Moreover, it exhibited equally large on current ($I_{on} > 1$ mA/μm) as multilayer phosphorene FETs, without any penalty of relatively lower DOS. On the other hand, the device performance of phosphorene TFETs is very susceptible to various material and device parameters such as number of layers, power supply voltage, channel length, and doping concentrations. Our comprehensive simulation results revealed that either bilayer or trilayer phosphorene can provide the best performance in TFET with the maximum I_{on}/I_{off} of 2×10^{11} and the SS as low as 13 mV/dec by engineering channel length, doping concentration and power supply voltage properly. Finally, we compared the performance of conventional FET and TFETs based on phosphorene, showing feasibility of each device for different target applications where different requirements are needed. Here we have provided irreplaceable insights into phosphorene-based FETs

through comprehensive optimization processes, which may also be extended to the engineering practice of other similar 2D semiconductor FETs.

Chapter 5 Conclusions and Future Work

5.1 Conclusions

In summary, in this thesis a novel black phosphorus and its potential for electronic devices are investigated. First, the performance limit of few-layer BP FETs was discussed. We presented simulations of bilayer phosphorene FETs using self-consistent atomistic quantum transport simulations. Our results exhibited that 10-nm-channel bilayer phosphorene FETs can achieve excellent device characteristics such as I_{on} > 3 mA/μm and SS ~66 mV/dec. While the scaling of gate dielectric monotonically improves the overall performance of the device, the channel length can be scaled down only to ~8 nm due to significant short-channel effects. Bilayer phosphorene FETs have favorable switching characteristics over other similar bilayer TMDC devices. The device performance of single-gate and double-gate structure was also compared. Simulation results suggested double-gate structure could improve both on-state and off-state device performance quite significantly, especially with a large EOT. We also investigated the effect of EOT variation. By using high-κ dielectric material, 229% higher transconductance and 30.4% smaller subthreshold swing could be achieved.

Next, design strategy towards different targets on high-performance and low-power applications based on BP was discussed in details. We explored mono- to pentalayer phosphorene FETs using self-consistent atomistic quantum transport simulations. We first examined the conventional FET structure and concluded that monolayer phosphorene can provide the best performance in every aspect. We showed that monolayer phosphorene FET can be switched near the classical limit of SS = 60 mV/dec with the large immunity to GIDL. Moreover, it exhibited equally large on current (I_{on} > 1 mA/μm) as multilayer phosphorene FETs, without any penalty of relatively lower DOS. On the other hand, the device performance of phosphorene TFETs is very susceptible to various material and device parameters such as number of layers, power supply voltage, channel length, and doping concentrations. Our comprehensive simulation results revealed that either bilayer or trilayer phosphorene can provide the best performance in TFET with the maximum I_{on}/I_{off} of 2×10^{11} and the SS as low as 13 mV/dec by engineering channel length, doping concentration and power supply voltage properly. Finally, we compared the performance of conventional FET and TFETs based on phosphorene, showing feasibility of each device for different target applications where different requirements are needed.

In this thesis, we have provided irreplaceable insights into phosphorene-based FETs through comprehensive optimization processes, which may also be extended to the engineering practice of other similar 2D semiconductor FETs.

5.2 Future Work

By using hetero-structure of monolayer and multilayer BP, we can further optimize the device performance of BP TFETs. TFETs are switched by modulating quantum tunneling barrier. At off state, tunneling current is blocked by thick barrier; at on state, a thin barrier makes large tunneling current possible. Since bandgap has a huge effect on device performance, device performance of TFETs can be optimized by using hetero-junction based on two materials of different bandgap [51]–[55]. For example, by properly using a hetero-structure of BP, we may get higher I_{on} but the I_{off} can remain unaltered. As BP shows significant layer number dependency in its bandgap, it provides a great opportunity to investigate effect of hetero-junctions. In addition, we may develop a better understanding on interlayer transport in layered materials by investigating various BP hetero-junctions structures.

Graphene is considered great potential in radio-frequency (RF) applications because of its extremely high mobility and long mean free path. Since the first demonstration in 2007 [56], various graphene RF FETs have been investigated and they exhibited large cutoff frequency (f_T) [57], [58]. However, it is revealed by researchers that graphene RF transistor may suffer from a few fundamental limitations that can restrict its high frequency performance. Since graphene is a zero bandgap material, the lack of current saturation can lead to compromised voltage and power gains in graphene RF transistors. As a result, most graphene RF FETs may suffer from much smaller maximum oscillation frequency (f_{max}) than f_T [59]. In this regards, semiconducting transition metal dichalcogenides are good candidates for RF applications, but due to the relatively lower mobility, it may show limited potential for high-performance RF transistors. On the other hand, BP shows a reasonably high carrier mobility and a wide tunable bandgap from 0.4 eV to 2 eV. Thin film BP RF transistors with gigahertz frequency operation have been demonstrated [60], [61], but theoretical investigation of monolayer and few-layer BP RF transistor is still absent. By using rigorous atomistic NEGF simulations, the potential of BP in RF application can be investigate, which will provide a new opportunity of BP for wireless communications.

Bibliography

[1]   K. S. Novoselov, A. K. Geim, S. V. Morozov, D. Jiang, Y. Zhang, S. V. Dubonos, I. V. Grigorieva, and A. A. Firsov, "Electric field effect in atomically thin carbon films," *Science*, vol. 306, no. 5696, pp. 666–669, 2004.

[2]   A. K. Geim, K. S. Novoselov, "The rise of graphene," *Nat. Mater.*, vol. 6, pp. 183–191, 2007.

[3]   S. Stankovich, D. A. Dikin, R. D. Piner, K. A. Kohlhaas, A. Kleinhammes, Y. Jia, Y. Wu, S. T. Nguyen, and R. S. Ruoff, "Synthesis of graphene-based nanosheets via chemical reduction of exfoliated graphite oxide," *Carbon N. Y.*, vol. 45, no. 7, pp. 1558–1565, 2007.

[4]   K. S. Kim, Y. Zhao, H. Jang, S. Y. Lee, J. M. Kim, K. S. Kim, J.-H. Ahn, P. Kim, J.-Y. Choi, and B. H. Hong, "Large-scale pattern growth of graphene films for stretchable transparent electrodes," *Nature*, vol. 457, no. 7230, pp. 706–710, 2009.

[5]   C. R. Dean, A. F. Young, I. Meric, C. Lee, L. Wang, S. Sorgenfrei, K. Watanabe, T. Taniguchi, P. Kim, K. L. Shepard, and J. Hone, "Boron nitride substrates for high-quality graphene electronics," *Nat. Nanotechnol.*, vol. 5, no. 10, pp. 722–726, 2010.

[6]   A. A. Balandin, S. Ghosh, W. Bao, I. Calizo, D. Teweldebrhan, F. Miao, and C. N. Lau, "Superior thermal conductivity of single-layer graphene," *Nano Lett.*, vol. 8, no. 3, pp. 902–907, 2008.

[7]   X. Wang, Y. Ouyang, X. Li, H. Wang, J. Guo, and H. Dai, "Room-temperature all-semiconducting sub-10-nm graphene nanoribbon field-effect transistors," *Phys. Rev. Lett.*, vol. 100, no. 20, pp. 100–103, 2008.

[8]   M. Y. Han, B. Ozyilmaz, Y. Zhang, and P. Kim, "Energy band-gap engineering of graphene nanoribbons," *Phys. Rev. Lett.*, vol. 98, no. 20, pp. 1–4, 2007.

[9]   K. F. Mak, C. H. Lui, J. Shan, and T. F. Heinz, "Observation of an electric-field-induced band gap in bilayer graphene by infrared spectroscopy," *Phys. Rev. Lett.*, vol. 102, no. 25, pp. 100–103, 2009.

[10]   C. H. Lui, Z. Li, K. F. Mak, E. Cappelluti, and T. F. Heinz, "Observation of an electrically tunable band gap in trilayer graphene," *Nat. Phys.*, vol. 7, no. 12, p. 10, 2011.

[11]   Z. H. Ni, T. Yu, Y. H. Lu, Y. Y. Wang, Y. P. Feng, and Z. X. Shen, "Uniaxial strain on graphene: Raman spectroscopy study and band-gap opening," *ACS Nano*, vol. 2, no. 11, pp.

2301–2305, 2008.

[12] F. Guinea, M. I. Katsnelson, and A. K. Geim, "Energy gaps and a zero-field quantum Hall effect in graphene by strain engineering - SI," *Nat Phys*, vol. 6, no. 1, pp. 30–33, 2010.

[13] G. Cocco, E. Cadelano, and L. Colombo, "Gap opening in graphene by shear strain," *Phys. Rev. B - Condens. Matter Mater. Phys.*, vol. 81, no. 24, pp. 1–4, 2010.

[14] L. Li, Y. Yu, G. J. Ye, Q. Ge, X. Ou, H. Wu, D. Feng, X. H. Chen, and Y. Zhang, "Black phosphorus field-effect transistors.," *Nat. Nanotechnol.*, vol. 9, no. 5, pp. 372–377, 2014.

[15] H. Liu, A. T. Neal, Z. Zhu, Z. Luo, X. Xu, D. Tománek, and P. D. Ye, "Phosphorene: An unexplored 2D semiconductor with a high hole mobility," *ACS Nano*, vol. 8, no. 4, pp. 4033–4041, 2014.

[16] H. Liu, Y. Du, Y. Deng, and P. D. Ye, "Semiconducting black phosphorus: synthesis, transport properties and electronic applications," *Chem. Soc. Rev.*, vol. 44, pp. 2732–2743, Oct. 2015.

[17] Q. H. Wang, K. Kalantar-Zadeh, A. Kis, J. N. Coleman, and M. S. Strano, "Electronics and optoelectronics of two-dimensional transition metal dichalcogenides.," *Nat. Nanotechnol.*, vol. 7, no. 11, pp. 699–712, 2012.

[18] J. Qiao, X. Kong, Z.-X. Hu, F. Yang, and W. Ji, "High-mobility transport anisotropy and linear dichroism in few-layer black phosphorus.," *Nat. Commun.*, vol. 5, p. 4475, 2014.

[19] A. N. Rudenko, S. Yuan, and M. I. Katsnelson, "Toward a realistic description of multilayer black phosphorus: From GW approximation to large-scale tight-binding simulations," *Phys. Rev. B*, vol. 92, no. 8, p. 085419, 2015.

[20] A. Castellanos-Gomez, "Black Phosphorus: Narrow Gap, Wide Applications," *J. Phys. Chem. Lett.*, vol. 6, no. 21, pp. 4280–4291, 2015.

[21] M. Buscema, D. J. Groenendijk, G. a Steele, H. S. J. van der Zant, and A. Castellanos-Gomez, "Photovoltaic effect in few-layer black phosphorus PN junctions defined by local electrostatic gating.," *Nat. Commun.*, vol. 5, p. 4651, 2014.

[22] Z. Wang, H. Jia, X. Zheng, R. Yang, Z. Wang, G. J. Ye, X. H. Chen, J. Shan, and P. X.-L. Feng, "Black phosphorus nanoelectromechanical resonators vibrating at very high frequencies," *Nanoscale*, vol. 7, no. 3, pp. 877–884, 2015.

[23] N. Youngblood, C. Chen, S. J. Koester, and M. Li, "Waveguide-integrated black phosphorus photodetector with high responsivity and low dark current," *Nat. Photonics*, vol. 9, no. April, pp. 249–252, 2015.

[24] S. Datta, *Quantum transport: atom to transistor*. Cambridge University Press, 2005.

[25] A. N. Rudenko and M. I. Katsnelson, "Quasiparticle band structure and tight-binding model for single- and bilayer black phosphorus," *Phys. Rev. B*, vol. 89, no. 20, p. 201408, 2014.

[26] K. Lam, Z. Dong, and J. Guo, "Performance limits projection of black phosphorous field-effect transistors," *IEEE Electron Device Lett.*, vol. 35, no. 9, pp. 936–965, 2014.

[27] F. Liu, Y. Wang, X. Liu, J. Wang, and H. Guo, "Ballistic Transport in Monolayer Black Phosphorus Transistors," *IEEE Trans. Electron Devices*, vol. 61, no. 11, pp. 3871–3876, 2014.

[28] J. Chang and C. Hobbs, "Theoretical study of phosphorene tunneling field effect transistors," *Appl. Phys. Lett.*, vol. 106, no. 8, p. 083509, 2015.

[29] R. Wan, X. Cao, and J. Guo, "Simulation of phosphorene Schottky-barrier transistors," *Appl. Phys. Lett.*, vol. 105, no. 16, p. 163511, 2014.

[30] R. Lake, G. Klimeck, R. C. Bowen, and D. Jovanovic, "Single and multiband modeling of quantum electron transport through layered semiconductor devices," *J. Appl. Phys.*, vol. 81, no. 12, pp. 7845–7869, 1997.

[31] M. P. L. Sancho, J. M. L. Sancho, and J. Rubio, "Highly convergent schemes for the calculation of bulk and surface Green functions," *J. Phys. F Met. Phys.*, vol. 15, no. 4, pp. 851–858, Apr. 1985.

[32] D. Yin and Y. Yoon, "Can bilayer black phosphorus outperform monolayer in field-effect transistors?," *Device Res. Conf. - Conf. Dig. DRC*, vol. 2015-August, no. 5, pp. 177–178, 2015.

[33] D. Yin, G. Han, and Y. Yoon, "Scaling Limit of Bilayer Phosphorene FETs," *IEEE Electron Device Lett.*, vol. 36, no. 9, pp. 978–980, 2015.

[34] V. Mishra, S. Smith, K. Ganapathi, and S. Salahuddin, "Dependence of intrinsic performance of transition metal dichalcogenide transistors on materials and number of layers at the 5 nm channel-length limit," in *Technical Digest - International Electron Devices Meeting, IEDM*, 2013, pp. 136–139.

[35] D. J. Late, T. Doneux, and M. Bougouma, "Single-layer MoSe2 based NH3 gas sensor," *Appl. Phys. Lett.*, vol. 105, no. 23, p. 233103, 2014.

[36] W. Bao, X. Cai, D. Kim, K. Sridhara, and M. S. Fuhrer, "High mobility ambipolar MoS2 field-effect transistors: Substrate and dielectric effects," *Appl. Phys. Lett.*, vol. 102, no. 2013, 2013.

[37] S. Das, H. Chen, A. V. Penumatcha, and J. Appenzeller, "High Performance Multilayer MoS_2 Transistors with Scandium Contacts.," *Nano Lett.*, vol. 13, no. 1, pp. 100–105, 2012.

[38] S. Das, H. Y. Chen, A. V. Penumatcha, and J. Appenzeller, "High performance multilayer MoS2 transistors with scandium contacts," *Nano Lett.*, vol. 13, no. 1, pp. 100–105, 2013.

[39] B. Radisavljevic, A. Radenovic, J. Brivio, V. Giacometti, and A. Kis, "Single-layer MoS_2 transistors.," *Nat. Nanotechnol.*, vol. 6, no. 3, pp. 147–150, Mar. 2011.

[40] A. V. Penumatcha, R. B. Salazar, and J. Appenzeller, "Analysing black phosphorus transistors using an analytic Schottky barrier MOSFET model," *Nat. Commun.*, vol. 6, p. 8948, 2015.

[41] X. Cao and J. Guo, "Simulation of phosphorene field-effect transistor at the scaling limit," *IEEE Trans. Electron Devices*, vol. 62, no. 2, pp. 659–665, 2015.

[42] F. Liu, Q. Shi, J. Wang, and H. Guo, "Device performance simulations of multilayer black phosphorus tunneling transistors," *Appl. Phys. Lett.*, vol. 107, no. 20, p. 203501, 2015.

[43] D. Yin and Y. Yoon, "Design strategy of two-dimensional material field-effect transistors: Engineering the number of layers in phosphorene FETs," *J. Appl. Phys.*, vol. 119, no. 21, p. 214312, 2016.

[44] Y. Du, H. Liu, and P. D. Ye, "Device Perspective for Black Phosphorus Field-Effect Transistors: Contact Resistance, Ambipolar Behavior, and Scaling," *ACS Nano*, vol. 8, no. 10, pp. 10035–10042, 2014.

[45] W. Y. Choi, J. Y. Song, J. D. Lee, Y. J. Park, and B.-G. Park, "70-nm impactionization metal-oxide-semiconductor (I-MOS) devices integrated with tunneling field-effect transistors (TFETs)," *Electron Devices Meet. 2005. IEDM Tech. Dig. IEEE Int. Washington, DC*, pp. 955–958, 2005.

[46] W. Y. Choi, B. Park, J. D. Lee, and T. K. Liu, "Tunneling Field-Effect Transistors (TFETs)

With Subthreshold Swing (SS) Less Than 60 mV / dec," *IEEE Electron Device Lett.*, vol. 28, no. 8, pp. 743–745, 2007.

[47]   T. NAGAHAMA, M. Kobayashi, Y. AKAHAMA, S. ENDO, and S. NARITA, "Optical Determination of Dielectric Constant in Black Phosphorus," *J. Phys. Soc. Japan*, vol. 54, no. 6, pp. 2096–2099, 1985.

[48]   S. O. Koswatta, M. S. Lundstrom, M. P. Anantram, and D. E. Nikonov, "Simulation of phonon-assisted band-to-band tunneling in carbon nanotube field-effect transistors," *Appl. Phys. Lett.*, vol. 87, no. 25, p. 253107, 2005.

[49]   H. Ilatikhameneh, Y. Tan, B. Novakovic, G. Klimeck, R. Rahman, and J. Appenzeller, "Tunnel Field-Effect Transistors in 2-D Transition Metal Dichalcogenide Materials," *IEEE J. Explor. Solid-State Comput. Devices Circuits*, vol. 1, pp. 12–18, 2015.

[50]   Y. Yoon and S. Salahuddin, "Barrier-free tunneling in a carbon heterojunction transistor," *Appl. Phys. Lett.*, vol. 97, no. 3, p. 033102, 2010.

[51]   E. H. Toh, G. H. Wang, L. Chan, G. Samudra, and Y. C. Yeo, "Device physics and guiding principles for the design of double-gate tunneling field effect transistor with silicon-germanium source heterojunction," *Appl. Phys. Lett.*, vol. 91, no. 24, pp. 0–3, 2007.

[52]   K. Ganapathi and S. Salahuddin, "Heterojunction vertical band-to-band tunneling transistors for steep subthreshold swing and high on current," *IEEE Electron Device Lett.*, vol. 32, no. 5, pp. 689–691, 2011.

[53]   L. Liu, D. Mohata, and S. Datta, "Scaling length theory of double-gate interband tunnel field-effect transistors," *IEEE Trans. Electron Devices*, vol. 59, no. 4, pp. 902–908, 2012.

[54]   S. O. Koswatta, S. J. Koester, S. Member, and W. Haensch, "On the Possibility of Obtaining MOSFET-Like Performance and Sub-60-mV / dec Swing in 1-D Broken-Gap Tunnel Transistors," *IEEE Trans. Electron Devices*, vol. 57, no. 12, pp. 3222–3230, 2010.

[55]   N. Gillgren, D. Wickramaratne, Y. Shi, T. Espiritu, J. Yang, J. Hu, J. Wei, X. Liu, Z. Mao, K. Watanabe, T. Taniguchi, M. Bockrath, Y. Barlas, R. K. Lake, and C. Ning Lau, "Gate tunable quantum oscillations in air-stable and high mobility few-layer phosphorene heterostructures," *2D Mater.*, vol. 2, no. 1, p. 011001, 2014.

[56]   I. Meric, N. Baklitskaya, P. Kim, and K. L. Shepard, "RF performance of top-gated, zero-

bandgap graphene field-effect transistors," *Tech. Dig. - Int. Electron Devices Meet. IEDM*, no. January 2009, 2008.

[57] P. Tassin, T. Koschny, and C. M. Soukoulis, "Graphene for terahertz applications," *Science (80-.).*, vol. 341, no. 6146, pp. 620–621, 2013.

[58] R. Cheng, J. Bai, L. Liao, H. Zhou, Y. Chen, L. Liu, Y. Lin, S. Jiang, and Y. Huang, "High-frequency self-aligned graphene transistors with transferred gate stacks," *Proc. Natl. Acad. Sci.*, vol. 109, no. 29, pp. 11588–11592, 2012.

[59] P. J. Tasker and B. Hughes, "Importance of Source and Drain Resistance to the Maximum fT of Millimeter-Wave MODFET's," *IEEE Electron Device Lett.*, vol. 10, no. 7, pp. 291–293, 1989.

[60] X. Luo, Y. Rahbarihagh, J. C. M. Hwang, H. Liu, Y. Du, and P. D. Ye, "Temporal and Thermal Stability of Al_2O_3-Passivated Phosphorene MOSFETs," *IEEE Electron Device Lett.*, vol. 35, no. 12, pp. 1314–1316, 2014.

[61] H. Wang, X. Wang, F. Xia, L. Wang, H. Jiang, Q. Xia, M. L. Chin, M. Dubey, and S. J. Han, "Black phosphorus radio-frequency transistors," *Nano Lett.*, vol. 14, no. 11, pp. 6424–6429, 2014.